Multi-phase Multi-dimensional Analysis of PEM Fuel Cells with Carbon Monoxide Poisoning and Oxygen Bleeding

by

Yaqun Li

A thesis
presented to the University of Waterloo
in fulfillment of the
thesis requirement for the degree of
Master of Applied Science
in
Mechanical Engineering

Waterloo, Ontario, Canada, 2010

©Yaqun Li 2010

AUTHOR'S DECLARATION

I hereby declare that I am the sole author of this thesis. This is a true copy of the thesis, including any required final revisions, as accepted by my examiners.

I understand that my thesis may be made electronically available to the public.

Abstract

Polymer electrolyte membrane (PEM) fuel cells are promising alternative green power source for mobile, portable and stationary applications. However, their cost, durability, and performance are impacted by their sensitivity to impurities in fuel stream. Carbon monoxide (CO), an impurity commonly present in the hydrogen gas produced from hydrocarbon fuels, is known to have a significant degrading effect on PEM fuel cell performance because CO has a strong affinity to the platinum-based catalyst. At present, most studies in literature are limited to either experimental or simplified-dimensional analysis/modeling. In this thesis research, a three-dimensional (3D) multiphase PEM fuel cell model with the CO poisoning and O_2 bleeding is developed based on the conservation laws for mass, momentum, energy, and species, and implemented in the commercial software Fluent (6.3.26) through the user-defined functions. Numerical simulations are conducted to simulate a single PEM fuel cell including flow channels, gas diffusion layers, catalyst layers, and PEM. The simulation results are compared with experimental data favorably. The result shows that the reaction rate of hydrogen in the anode catalyst layer is higher near the membrane layer, decreasing towards the gas diffusion layer (GDL) interface, and the reaction rate in general is higher in the inlet region and decreases towards the exit region of the flow channel. It means that the outlet of anode catalyst layer next to the flow channel and GDL has suffered the most significant poisoning effect. The result helps optimize the design of anode catalyst layer by embedding more platinum on the most poisoned area to increase available surface for hydrogen adsorption; similarly, reducing platinum loading on the less poisoned area. The fuel cell performance can be almost fully recovered when switching the anode fuel mixture to pure hydrogen, though it takes a long period of time. The reaction rate of hydrogen decreases significantly along the flow channel when impurity mixture is provided; while there is little change along the channel for pure hydrogen fuel. Adding oxygen into the anode fuel mixture can mitigate CO poisoning, but there is a time delay when the oxygen is introduced into the anode stream and when the performance starts to recover. It is observed that at the beginning of oxygen introduced in the anode stream the recovery rate in the region adjacent to the channel outlet is faster than the rate in the region close to the inlet. This difference in the recovery rate gradually becomes smaller over time. In addition, the influence of CO poisoning and oxygen bleeding on multi-phase water is investigated. The influence on dissolved water is only clearly seen in the anode catalyst layer next to the land area. Finally, response to sudden load changes is simulated by changing cell voltage. It is found that the overshoot and undershoot are more significant at high current densities.

Acknowledgements

I would like to express my deepest gratitude to my supervisor, Dr. Xianguo Li, for his invaluable guidance, steady encouragement, inspiration and support throughout my work.

I would like to thank Dr. Hao Wu, Nada Zamel, Dr. Yi Ren, Kui Jiao, and Violeta Popov, for their help in writing and computer support.

The financial support of the Natural Sciences and Engineering Research Council of Canada (NSERC) and Auto21 NCE Program is gratefully acknowledged.

Table of Contents

AUTHOR'S DECLARATION ii
Abstract iii
Acknowledgements iv
Table of Contents v
List of Figures vii
List of Tables ix
List of Symbols x
Chapter 1 Introduction 1
1.1 Background 1
1.2 Objectives 4
1.3 Scope and Outline of the Thesis 4
Chapter 2 Literature Review 6
2.1 Fuel Contaminants 6
2.2 Experiments 8
2.3 Numerical Models 10
2.4 Summary 11
Chapter 3 Model Formulation 13
3.1 Governing Equations 13
3.1.1 Conservation of Mass 14
3.1.2 Conservation of Momentum 14
3.1.3 Conservation of Species 14
3.1.4 Multi-water Phase Transport 14
3.1.5 Conservation of Energy 15
3.1.6 Conservation of Charge 15
3.1.7 Coverage of Species on Anode Catalyst Layer 16
3.2 Reaction Kinetics 18
3.2.1 Hydrogen Reaction Rate 19
3.2.2 Carbon Monoxide Reaction Rate 19
3.2.3 Oxygen Reaction Rate 20
3.3 Boundary and Initial Conditions 22
Chapter 4 Numerical Implementation 25

4.1 Numerical Procedure 25
4.2 Grid Independent Solution 26
Chapter 5 Results and Discussion – Part I: Steady State 27
5.1 Validation of Steady State Model 27
5.2 Effect of CO Concentration on Fuel Cell Performance 28
5.3 Effect of CO Poisoning in 3D Distribution 30
5.4 Effect of Oxygen Bleeding 37
5.5 Effect of CO Poisoning and Oxygen Bleeding on Multi-phase Water 41
Chapter 6 Results and Discussion – Part II: Transient State 44
6.1 Validation of Transient Model 44
6.2 Effect of CO Concentration on Fuel Cell Performance 45
6.3 Effect of Cell Voltage on Fuel Cell Performance 49
6.4 Recovery of Fuel Cell Performance 52
Chapter 7 Conclusions and Recommendations 56
Bibliography 57

List of Figures

Figure 1.1 Schematics of (a) a single PEMFC [4] and (b) a PEMFC stack with three single cells 2
Figure 1.2 Schematic of the CO adsorption process on the platinum catalyst 3
Figure 3.1 Schematic of Modeling Domain 13
Figure 5.1 Comparison of the cell performance predictions with the experimental results. The points represent actual experimental results [105], and the curves represent simulations based on the model developed. 27
Figure 5.2 Model predictions of anode overpotential changing with current density 28
Figure 5.3 Model predictions of species' coverage on anode catalyst layer changing with CO concentration 29
Figure 5.4 Model predictions of species' coverage on anode catalyst layer changing with current density when 20 ppm CO is added into anode fuel feed 30
Figure 5.5 (a) Mass fraction of hydrogen; (b) Mass fraction of CO; (c) Mass fraction of H_2O. (Mass fraction distributions in anode catalyst layer when anode fuel is contaminated by 20 ppm CO) 31
Figure 5.6 (a) Mass fraction of hydrogen with pure hydrogen; (b) Coverage of hydrogen with pure hydrogen; (c) Coverage of hydrogen with 20 ppm CO; (d) Coverage of CO with 20 ppm CO. (Distribution in anode catalyst layer) 32
Figure 5.8 Adsoprtion rate ($c/m^3.s$) of CO in anode catalyst layer with CO contaminants in the anode fuel gas stream (a) 5 ppm; (b) 20 ppm; (c) 50 ppm; (d) 100 ppm. 34
Figure 5.9 (a) Reaction rate ($c/m^3.s$) of hydrogen; (b) Reaction rate of CO; (c) Temperature distribution. (with 20 ppm CO, the contour is on anode catalyst layer) 36
Figure 5.10 Distribution of anode overpotential (V). (with 20 ppm CO, the contour is on anode catalyst layer) 37
Figure 5.12 (a) Pt-H; (b) Pt-CO; (c) Pt-O; (d) H_2-O_2 oxidation reaction rate ($c/m^3.s$); (e) CO-O_2 oxidation rate ($c/m^3.s$).(100 ppm CO+0.5% O_2, the contours are on anode catalyst layer) 40
Figure 5.13 Dissolved water in anode catalyst layer (top), membrane (middle), and cathode catalyst layer (bottom) when anode fuel is supplied with (a) pure hydrogen; (b) mixture fuel with 100 ppm CO; (c) mixture fuel with 100 ppm CO and 0.5% oxygen 42
Figure 6.1 Current at 0.6 V during the poisoning process vs. time for two different anode feed gas compositions. The points represent actual experimental results [93], and the curves represent simulations based on the model developed 44
Figure 6.2 The coverage of hydrogen on anode catalyst layer 45

Figure 6.3 The coverage of CO on anode catalyst layer 46
Figure 6.4 The adsorption/desorption rates and electro-oxidation rate of hydrogen on anode catalyst layer 47
Figure 6.5 The adsorption/desorption rates and electro-oxidation rate of CO on anode catalyst layer 47
Figure 6.6 The electro-oxidation rate of hydrogen in anode catalyst layer ($c/m^3.s$) 48
Figure 6.7 Current density changes according to cell voltage 49
Figure 6.8 Anode overpotential changes according to cell voltage 50
Figure 6.9 Coverage of CO changes according to cell voltage 51
Figure 6.10 Coverage of hydrogen changes according to cell voltage 52
Figure 6.11 The change of current density according to anode fuel feed switches 53
Figure 6.12 The 3D distribution of hydrogen electro-oxidation rate ($c/m^3.s$) in anode catalyst layer according to time steps used in Figure 6.11 54
Figure 6.13 The recovery of hydrogen electro-oxidation rate ($c/m^3.s$) in anode catalyst layer when 0.5% O_2 is added into anode mixture fuel with 100 ppm CO 55

List of Tables

Table 3.1 Physical and operating parameters used in model [57, 83, 107] 16
Table 3.2 Source terms in conservation equations [7] 17
Table 3.3 Kinetic parameters used in this model [103] 21
Table 3.4 Kinetic parameters in former models [40, 54, 93] 22
Table 3.5 Kinetic parameters in former models [57] 22

List of Symbols

Letters

a	water activity
A	Active reaction area (m^2)
C	molar concentration (mol/m^3)
c_p	specific heat (J/kg.K)
D	mass diffusivity of species (m^2/s)
EW	equivalent weight (1.1 kg/mol)
F	Faraday's constant 96487 (C/mol)
R	gas constant 8.314 (J/K.mol)
I	current density (A/cm^2)
k	permeability (m^2)
m	mass flux (kg/m^2 .s)
n_d	electroosmotic drag coefficient
P	pressure (kPa)
RH	relative humidity
s	saturation
S	source terms
t	time (s)
T	temperature (K)
u	Velocity (m/s)
V	volume (m^3)
q	adsorption/desprtion/oxidation rate (c/m^3.s)
K	adsorption/oxidation rate constant
B	desorption rate constant
r	interaction parameter 3.97×10^4 (J/mol)
E	activation energy

Greek letters

ε	porosity
η	overpotential (V)
λ	membrane water content
ρ	density (kg/m^3)
σ	electric conductivity (S/m)
θ	species coverage in anode catalyst layer
ξ	Stoichiometric ratio
β	symmetry factor 0.05

Subscripts and superscripts

a	anode
c	cathode
cell	cell characteristic
eff	effective value
g	gas phase
i	the ith species
m	membrane phase; membrane
ref	reference state
rev	reversible
s	solid phase

Chapter 1
Introduction

1.1 Background

Due to their low pollution and high energy efficiency characteristics, fuel cells are widely regarded as promising alternative green power generation devices that will help meet societal goals of climate stability, renewable energy supplies and zero-emission transportation. They can be used to power cars, plants, residences, or even laptops [1-3]. Generally, fuel cells can be classified by the type of electrolyte used, such as the alkaline fuel cell, phosphoric acid fuel cell, molten carbonate fuel cell, solid oxide fuel cell, Polymer electrolyte membrane (PEM) fuel cell, and so forth. PEM fuel cell is considered to be the most appropriate type for vehicle application due to its relatively low operating temperatures, stable solid-phase electrolyte, and high power density.

Thus, the fuel cell used in this work is PEM fuel cell, which is divided into seven layers. The central layer – PEM is sandwiched between catalyst layers. Although the catalyst layer is only about 10 μm thick, electrochemical reactions only take place in this section; especially with the CO-poisoning reaction and heterogeneous oxidation reactions with oxygen. Also, in order to maximize the reaction efficiency and minimize the cost, the 3D simulation results can help to optimize the distribution of platinum particles, because electrochemical reactions and poisoning phenomena are not evenly distributed over the catalyst layer. Gas diffusion layers are playing important roles in the heat and water management of the fuel cell. They have typical thicknesses between 200 and 300 μm. In addition, bipolar plates are ignored in this model by choosing high stoichiometric ratios to provide enough reactant gases and by applying a reasonable boundary condition.

In Figure 1.1, schematics of a PEM fuel cell stack and a single PEM fuel cell are given. In a single PEM fuel cell, hydrogen is provided to anode channel, while oxygen is provided to cathode channel. The electro-chemical reaction on anode side can be written as: $H_2 \rightarrow 2H^+ + 2e^-$. The hydrogen is oxidized at the anode/electrolyte interface into proton H^+ and electron e^- . The protons migrate through the electrolyte membrane, while the electrons are transported through an external circuit. On the cathode side, the migrated protons and electrons react with adsorbed oxygen, forming water the as: $\frac{1}{2}O_2 + 2H^+ + 2e^- \rightarrow H_2O$. In short, the overall electro-chemical reaction within PEM fuel cell can be formulated as the following equation: $H_2 + \frac{1}{2}O_2 \rightarrow H_2O + Electrical\ Energy + Heat$.

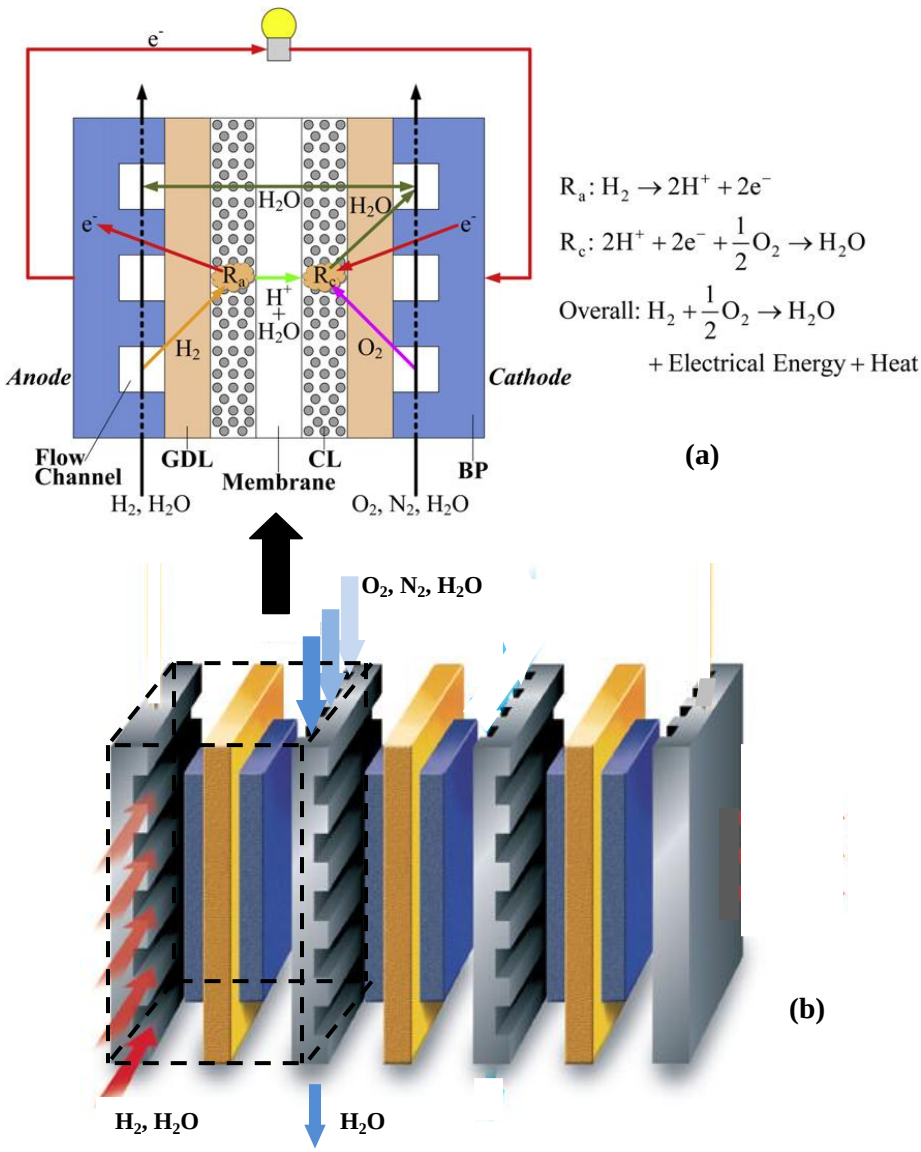

Figure 1.1 Schematics of (a) a single PEMFC [4] and (b) a PEMFC stack with three single cells

However, several technical challenges, such as cost, durability and performance improvement must be overcome before its widespread commercialization. These technical issues are significantly influenced by the PEM fuel cells' sensitivity to the quality of hydrogen fuels.

Since the costs associated with the clean-up process of the hydrogen fuel and its problematic storage, hydrogen fuel is usually obtained from natural gas steam reforming or liquid hydrocarbons by using an onboard reformer. Thus, reformers may give off contaminants (like CO, CO_2, H_2S) reducing the

environmental benefits that fuel cells may have, as well as severely degrading the fuel cell performance and durability [5].

This work is only focused on CO impurity, which has the most severe influence. The reformate feed gas may contain up to 2.5% CO by volume, which can be reduced to about 50 ppm CO using a selective oxidizer [6]. However, CO poisoning is considered as a site-elimination effect for hydrogen adsorption, which has significant degradation on fuel cell performance even in small amounts. In a CO-contaminated fuel feed, the bond of Pt=CO is much stronger than the bond of Pt-H, so that the CO will dominate the catalyst surface and push the hydrogen away as shown in Figure 1.2. The CO can be adsorbed onto either a bare platinum site or a Pt-H site as the following equations (1.1) and (1.2) [3].

$$CO + Pt \rightarrow Pt = CO \tag{1.1}$$

$$2CO + 2(Pt - H) \rightarrow 2(Pt = CO) + H_2 \tag{1.2}$$

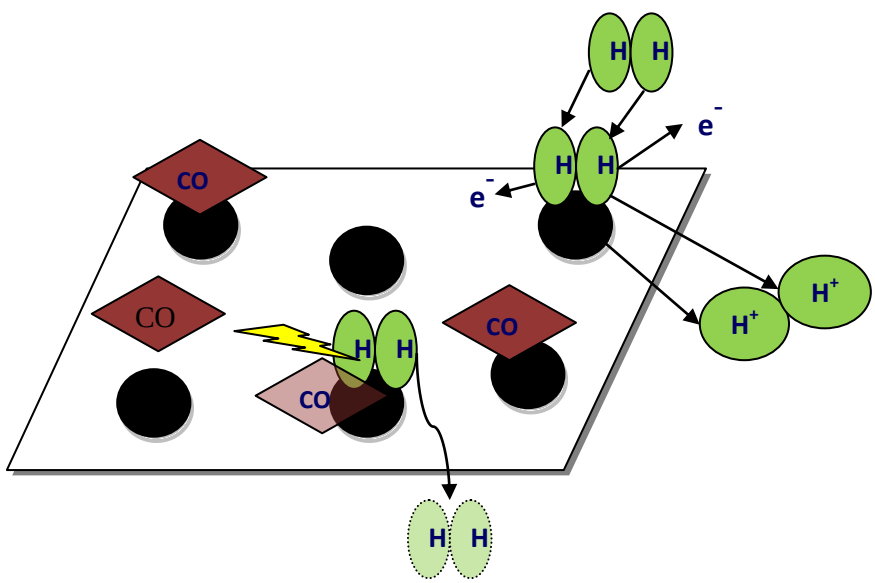

Figure 1.2 Schematic of the CO adsorption process on the platinum catalyst

Hence, many experimental studies have been carried out to investigate CO poisoning and its mitigation techniques. Nevertheless, the combination of various spatial and temporal scales makes it extremely challenging to conduct in-situ measurements or other observations through experimental means. Worse still, the laboratory experiment can be very expensive and time consuming, depending on the system

complexity. Therefore, mathematical models are becoming an important tool in revealing the underlying electrochemical dynamics and transport phenomena within fuel cells [7].

There are some numerical simulation studies about PEM fuel cell with CO poisoning in literature. Nevertheless, most of these works are 1D or 2D. Moreover, most works in 3D ignored the multi-phase water transport, which is one of the important phenomena in PEM fuel cells. Worse still, most studies are focused on steady state phenomena, so that the transient transport processes are usually overlooked.

1.2 Objectives

The objectives of this work are:

1. to better understand the 3D spatial distribution of the reaction rates in a PEM fuel cell with CO poisoning;
2. to investigate the transient response to sudden load changes when the PEM fuel cell has been poisoned by CO; and
3. to study the recovery of performance by oxygen bleeding.

Therefore, a multi-phase, multi-dimensional mathematical model is developed, and this model takes into account CO poisoning and oxygen bleeding effect at both steady and transient states.

1.3 Scope and Outline of the Thesis

This thesis focuses on developing a physical model to simulate the performance of a PEM fuel cell with the effect of CO poisoning and oxygen bleeding. The model is developed based on a set of governing equations for conservation of mass, momentum, energy, species and charged particles within the cell, with the species coverage on the anode catalyst layer. The electrochemical kinetics of the reactions within the cell is dealt with as a Butler-Volmer type relation. It should be noted that the simulated results of this thesis are mainly focused on the anode catalyst layer, since the CO and oxygen are both added into the anode fuel stream, and the poisoning and recovering reactions are constrained within the anode catalyst layer.

A literature review is presented at first. It addresses a summary of the current works in the experiments and numerical models about PEM fuel cell, especially with the consideration of CO poisoning and ways to mitigate of the poisoning.

The model formulation chapter describes the governing equations, reaction kinetics, and appropriate boundary and initial conditions for the given equation set. The boundary conditions are specified on the outer surfaces of a single PEM fuel cell domain. The initial conditions are set either to zero or a steady-state from a previous operating point.

The numerical implementation chapter includes details about the numerical procedure and research on grid independent solutions. Fluent (6.3.26) software is used in this work with the set of governing equations. The user defined functions is coded in terms of Language C. Moreover, some controlling strategies and under-relaxation schemes are also developed. In short, the solver and discretization scheme work properly.

The results are divided into two parts. The first part is focused on the steady state, which can help us to gain a basic knowledge of the physical model about cell performance, degradation, and the distribution of underlying reactions inside of the anode catalyst layer. Next, the second part is mainly about the transient behavior of fuel cell, simulating realistic scenarios, like the sudden change of road conditions. Hence, the effects of CO concentration on dynamic response time, the effects of sudden change of cell voltage, and the reversibility of fuel cell performance are all studied in chapter 6.

In summary, the combination of various spatial and temporal scales makes the model a unique tool for accurately describing the phenomena occurring in a PEM fuel cell with a focus on CO poisoning and oxygen bleeding process. Thus model will be extremely helpful for increasing a PEM fuel cell's durability and performance, while reducing cost as optimizing cell's design.

Chapter 2
Literature Review

2.1 Fuel Contaminants

Fuel cells have been used widely as their power could vary from a few watts which is suitable for portable applications, up to one million watts for some power plant as stationary applications [7]. More detailed works about the application of PEM fuel cells are illustrated in [8, 9].

However, due to the high cost of providing pure hydrogen, reformate fuel is usually supplied instead of pure hydrogen. Thus, a variety of contaminants in the anode fuel stream are unavoidable, such as, CO, CO_2, and H_2S. Numerous articles on the subject of contamination on PEM fuel cell show that even a small amount of impurities in the fuel stream could severely degrade the fuel cell's performance [3, 10-28].

CO is recognized as the crucial impurity in the fuel stream. Wilson et al. [29] concluded that compared with the use of pure hydrogen, the maximum power density is more than halved in the presence of only 5 ppm CO. This is because the stronger affinity of CO for platinum catalyst layer as compared with hydrogen, the existence of CO in the anode side will block the active sites of the anode catalyst layer which leads to a shortage of catalyst sites for hydrogen.

The degradation phenomena have been proved in many studies [12, 25-28] and it is found that the effect is strongly related to the CO concentration [31], the poisoning time [32, 33], the cell operation temperature [34, 35], and the anode catalyst types [24, 36-39]. Furthermore, the CO poisoning could also be affected by anode flow velocity and gas diffuser porosity. Zhou and Liu [40] state that under enough hydrogen supply, lower flow speed leads to better performance, since high velocity would bring in more CO to overshadow the effect of more hydrogen. Also, the result acquired in [41] shows that better performance of fuel cell is achieved when the lower porosity is applied, even with a limit reduction.

In addition, the influence of CO impurities would be amplified by the dilution of the anode fuel feed. Tao et al. [42] proved that hydrogen dilution effects by other inert gases such as nitrogen or carbon dioxide, the lower performance compared with pure hydrogen feed was observed; however, CO_2-diluted H_2 gives significantly larger polarizations than N_2-diluted H_2 for a PEM fuel cell with a Pt anode. Moreover, the negative effect is enhanced by increased dilution [43].

Worse still, the CO impurities can cross over the membrane through pin-holes, resulting in a severe impact on cathode performance [11]. It is surprising to see that the performance loss of the cathode sometimes could be more than that of the anode. Qi et al. [11] suggested some ways to reduce this poisoning effect by controlling membrane humidification, gas pressure difference between cathode side and anode side, thicker membrane structure, or applying CO-tolerant cathode catalysts.

CO_2 is another contaminant in reformate fuel. Smolinka et al [14] addressed that CO_2 reduction proceeds by reaction with adsorbed hydrogen rather than by reaction with dissolved hydrogen. Particularly, the hydrogen oxidation reaction (HOR) is affected by the decrease in hydrogen partial pressure due to the dilution effect of CO_2. But in reformate where CO is present beside CO_2, then CO_2 poisoning will have the largest effect if the stream contains CO trace impurities and the current density is relatively low [22]. Because CO_2 can be catalytically converted into CO, then poisons the catalyst. There are two theories about how this CO is formed. The first one claims that CO_2 reacts according to the so-called reverse water-gas shift reaction (RWGS) [13, 23]:

$$CO_2 + 2Pt - H_{ads} \rightarrow Pt - CO_{ads} + H_2O + Pt \tag{2.1}$$

The other one is that CO_2 reacts in an electrochemical reduction reaction [23]:

$$CO_2 + 2H^+ + 2e^- + Pt \leftrightarrow Pt - CO + H_2O \tag{2.2}$$

Ralph and Hogarth [24] showed that CO_2 forms a CO-like poison on both Pt/C and PtRu/C and concluded that the reaction occurred predominantly by electrochemical reduction (2.2). In this water-gas shift reaction, the significant performance loss has been proved by works [13, 23, 24]. Moreover, during the reaction, both temperature and the water content of the anode feed are believed to be very important parameters; however, since the kinetics of CO_2 electro-reduction are very slow, CO_2 is still considered a weak anode poison [16].

Finally, hydrogen sulfide has long been regarded as a strong fuel impurity for fuel cells [10, 17-20]. Uribe and Zawodzinski [21] reported that even at a level of 1 ppm, H_2S in the fuel stream could result in the completely failed performance within 20 hours. Mohtadi et al. [19] experimentally investigated that the H_2S poisoning can be partially recovered and the degree of the recovery is influenced by the electrochemical oxidation of the surface species.

As mentioned above, CO is recognized as the crucial impurity in fuel stream. Consequently, this work is focused on research of CO, and the analysis of CO_2 and H_2S are left for future work.

In order to mitigate CO poisoning effect, a variety of techniques have been developed to improve cells' performance; such as increasing fuel cell operating temperature, using Pt alloy material as an anode catalyst or designing a composite anode catalyst layer, and adding oxygen into the anode fuel.

Increasing PEM fuel cell operating temperature is an easy way to mitigate CO poisoning; however, a high temperature-tolerant membrane is needed [46, 51, 52].

Some works have been done on the use of CO-tolerant electrocatalysts [44-46]. Urian et al. [47] investigated for Pt, Pt-Ru (1:1) and various atomic ratios of supported Pt:Mo electrocatalysts in PEM fuel cells. Pt/Ru is considered to be the best H_2/CO oxidation catalyst, due to the CO-Ru bond is much stronger than the CO-Pt bond. Besides, other alloys like Pt/Sn and Pt/Mo, etc. have also been studied.

Yu et al. [48] and Wan et al. [49] brought up an idea of a composite anode for CO tolerant PEM fuel cells, i.e. the inner catalyst layer should be rich in platinum and the outside catalyst layer should be rich in CO tolerance electrocatalyst E.g. PtRu/C. Since the CO impurity could be electro-oxidized in the outer catalyst layer, then the hydrogen oxidation reaction has high activity in the inner catalyst layer without much cost. Meanwhile, Shi et al. [50] also suggested a novel anode which consists of placing Pt or Au particles in the diffusion layer. Thus, the electro-oxidation of CO occurs at Pt or Au particles at diffusion layer before it reaches the anode catalyst layer.

Last but not least, the use of oxygen or air bleeding has been shown to be the most effective mitigation method for CO poisoning [40, 54-59]. S. Gottesfeld and J. Pafford [59] assumed that the gas phase oxidation of CO and H_2 by oxygen is negligible; thus the oxidation is described by heterogeneous catalysis. Moreover, the use of hydrogen peroxide (H_2O_2) could also been successfully used to mitigate the level of CO [46]. The main advantage for the use of H_2O_2 as opposed to oxygen bleeding is that H_2O_2 has none of the safety problems associated with mixing hydrogen and oxygen gas [36].

In order to improve the fuel cell performance and durability, there are many studies that have been carried out to investigate CO poisoning and its mitigation technique – oxygen bleeding. The studies are mainly divided into two groups: experimental studies and numerical studies.

2.2 Experiments

Experimental results provided reproducible data suitable for verification of numerical models of poisoning and recovery behavior, as well as expanding the base of available steady-state and transient data useful to designers of control schemes and processing systems [52]. The phenomenon of CO poisoning has been studied extensively in literature; see [30, 44-54, 60-62]. On the anode side, the

presence of CO in the fuel stream results in severe degradation of the cell performance and is a kinetic effect [10]; also, it varies with time and position within the catalyst layer [11, 52, 63-72].

Wagner and Gulzow [73] focus on the electrochemical characterization, such as current-voltage-measurement and time resolved electrochemical impedance spectroscopy of PEM fuel cells during CO poisoning. The progressive poisoning was monitored using time resolved electrochemical impedance spectroscopy. Hence, the impedance spectra acquired can reflect the state of the fuel cell.

In Ref. [74] and [75], the enhanced mathematical techniques are used to suggest that the influence of CO on the electrochemical behavior of the contaminated fuel cell may be interpreted by means of a Faraday impedance in addition to potential-dependent hindrance of the charge transfer.

Another experimental method using a polymer membrane combined with a gold wire was suggested for performing a quantitative evaluation, and the result shows remarkable anode overpotential [76].

Some other experiments involving the PEM fuel cell exposed to CO poisoning are studied to improve the design of reformate fuel processing systems and control schemes to prevent CO transients.

The effects of operating conditions on cell performance are analyzed in [52]. Data is reported for Membrane Electrode Assemble (MEA) exposed to relatively high concentrations (500, 3000, 10000 ppm) of CO in hydrogen. A large amount of CO contaminant could speed up the poisoning process. The results show that poisoning rates are substantially lowered with an increase in pressure (up to four times) and temperature (up to fourteen times) [52]. The improvement of cell performance by increasing temperature is also proved in [20]. The permeability of gas diffusion media (GDM) is found out that it will also affect CO poisoning through the observation of poisoning and recovery rates for two types of gas diffusion media: single-sided ELAT and CARBEL CL GDM [58]. In addition, the residence time within fuel cell is another key factor in determining the extent of CO poisoning, and the flow rate of fuel feed has a big influence of the distribution of species [65]. Two other approaches to improve the cell performance are compared experimentally in [35]. Improved electrocatalysts for the anode such as PtRu alloys can significantly enhance the CO tolerance, yet the long term stability of such alloy catalysts is still an open question. In addition, the oxidation of CO by active oxygen decomposed from H_2O_2 leads to a great recovery of the cell performance.

In order to study the decay and recovery rates when the surface is exposed to equilibrium or pseudo-steady-state coverage, experiments consisted of both steady-state and transient measurements [58]. However, the rates cannot be measured under non-equilibrium state. Worse still, the reaction rates are too

fast to be measured with the equipment in the case of air bleed and 500 ppm CO/H_2. Consequently, numerical models are needed to solve these problems.

2.3 Numerical Models

Numerical modeling is extremely important and necessary to reveal the underlying electrochemical dynamics and transport phenomena within fuel cells. In literature, some mathematical models have been developed as well [77-84].

Pioneering models of Bernardi and Verbrugge [89, 90] and Springer et al. [79, 91] are only 1D in the analysis of the processes in the gas flow channels and the MEA. They are both assumed to be operated at steady state and be isothermal. A model containing both empirical and mechanistic parameters and evolving from a steady state electrochemical PEM fuel cell model is also developed in [30]. But the simulation at steady state could not provide the insight of transient transport phenomena. During acceleration and deceleration when the fuel cell is applied to land-based vehicles, many transient dynamic mechanisms become significant, while simple empirical models are unable to represent the transient dynamics [85]. Furthermore, because of the heat generation resulting from internal reactions, treating the fuel cells as isothermal is unreasonable.

Some other 1D mathematical models are more focused on methods to mitigate CO poisoning. In [70], several physical parameters are considered to promote CO tolerance and their influence on the response time. Also, oxidant-bleeding, self-oxidation, and current-pulsing methods are compared in the work. To improve fuel cell electrode performance by controlling electrode structure parameters, a model which describes the performance of electrodes formed by imbedding catalyzed carbon particles that are bonded to a membrane of a proton conductive polymer is applied with macro-homogeneous porous electrode theory [88]. Moreover, the current density equation in the work is written simply by multiplying i^0 with a factor of$(1-\theta_{CO})^2$, ie, $i_{CO}^0 = i^0(1-\theta_{CO})^2$ [88], which is inaccurate.

There are also some dynamic models [85-87]. Sedghisigarchi et al. [87] built a dynamic transient solid-oxide fuel cell by using Matlab; while Pukrushpan et al. [86] simulated the fuel cell stack, as well as external sub-systems, including compressor, supply manifold, static air cooler and static humidifier using Matlab software. However, these models are only useful in analyzing the overall performance of fuel cells, and the differential equation approach is limited mainly to a 1D analysis, which cannot be used to provide insight into the underlying transport and electrochemical phenomena that occur inside the fuel cells.

There are also some 2D and 3D models have been developed in literature. Zamel and Li [57] used COMSOL software to develop a 2D transient mathematical model to analyze how CO poisoning could affect the performance of a PEM fuel cell and influences of changing operating conditions. Wang and Wang [68] extended the single-domain model of Um et al. [92] to a 3D and transient single-phase model to study the transient dynamics of PEM fuel cells operation along with theoretical estimation of various time constants. The transient model is numerically implemented into Star-CD, a commercial CFD software, based on its users coding capacity [68]. In 3D fuel cell transient models [54, 93], the combined effects of trace quantities of CO and hydrogen dilution have been simulated at various time steps throughout the poisoning process, but the CO electro-oxidation term has been neglected due to its relatively small magnitude.

In literature, 3D models reported are mostly developed using commercial computational fluid dynamic (CFD) codes. These models provide comprehensive details on the distribution of distribution of reactants and allow sensitivity analysis and prediction of performance under various conditions, but they do not account for phase change and liquid water concentration in the electrode [94]. So is the work in [83], Wu et al. concentrated on the two-fluid model including dissolved water is in membrane, as well as, liquid water is in the cathode side, which ignores the water vapor introduced by humidified fuel. Therefore, a multi-dimensional PEM fuel cell model is needed to give us detailed spatial distributions of underlying reactions within PEM fuel cells, and the model is more comprehensive when multi-phase water are considered.

2.4 Summary

In summary, as long as CO poisoning effects are concerned, the modeling domain the previous models used are usually simplified with either reduced dimensions (1D or 2D) or reduced components related to modeling, let alone the transient state study. Therefore, the finite-rate adsorption/desorption process are usually neglected in previous models [96]. Most of the dynamic modeling was carried out at the system level, using a performance model where the underlying transient phenomena within the PEM fuel cell are of no concern [7]. Moreover, the dynamic transition among multi-water phases (dissolved, liquid, and vapor) and non-isothermal effects imparting the cell dynamic performance with CO poisoning are still rarely touched [7].

This study has resolved most of the shortcomings left by former studies. It can help us to uncover underlying transient transport phenomena within PEM fuel cells to predict the PEM fuel cells'

performance. Thus, the simulation results can help us to optimize fuel cells' performance and stability, as well as, minimize costs.

Chapter 3
Model Formulation

The modeling domain considered in this study as shown in Figure 3.1, is composed of straight flow channels, gas diffusion layers, catalyst layers, and a polymer electrolyte membrane. Since the platinum catalyst has strong affinity to CO, the anode catalyst layer is always poisoned by CO contaminant if the fuel is derived from hydrocarbon fuel. Thus, the research of this work is more focused on the anode catalyst layer. Firstly, some assumptions have been made before the model formulation. Gravity effects are ignored; the gas reactants are ideal gases; the gas flow in the channel is laminar flow; no other contamination effects are considered except for CO; no gas species crossover the membrane [7].

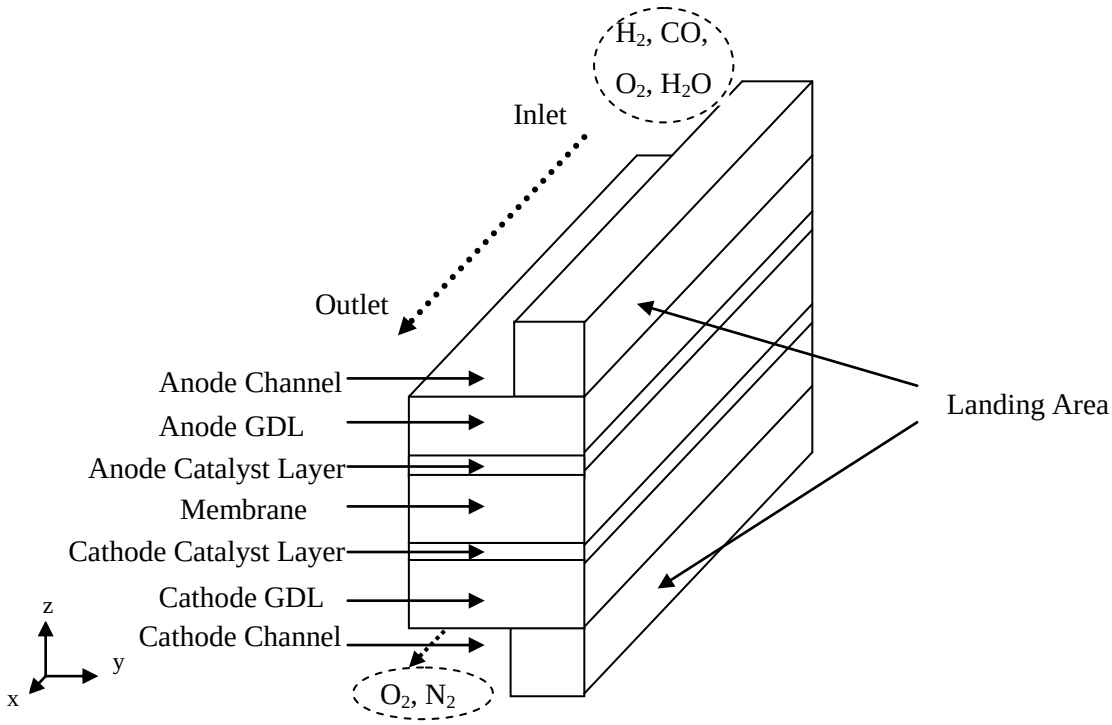

Figure 3.1 Schematic of Modeling Domain

3.1 Governing Equations

In this study, transport of gases, electrons, protons, momentum and heat is considered in all the components of the cell (flow channels, gas diffusion layers, catalyst layers and electrolyte membrane) at

both steady and transient states. The complete set of governing equations for the multi-dimensional multi-phase transport is given below, and all the effects are coupled:

3.1.1 Conservation of Mass

$$\frac{\partial}{\partial t}\left(\varepsilon^{\text{eff}}\rho_g\right) + \nabla \cdot \left(\rho_g \vec{u}_g\right) = S_m \tag{3.1}$$

where S_m stands for the mass sourcewhich depends on the cell region. The mass source term for hydrogen in the anode catalyst layer is expressed as: $R_a = q_{H_ox} A_v F$. q_{H_ox} is electro-oxidation rate of hydrogen. Moreover, $\rho_g, \vec{u}_g$ are the superficial values of the density and velocity, respectively; $\varepsilon^{\text{eff}} = \varepsilon(1-s)$ is the effective porosity for gas phase transport, ε is the bulk porosity of the materials, and s is the liquid saturation.

3.1.2 Conservation of Momentum

$$\frac{\partial}{\partial t}\left(\frac{\rho_g \vec{u}_g}{\varepsilon^{\text{eff}}}\right) + \nabla \cdot \left(\frac{\rho_g \vec{u}_g \vec{u}_g}{\left(\varepsilon^{\text{eff}}\right)^2}\right) = -\nabla P_g + \nabla \cdot (\bar{\bar{\tau}}) + S_u \tag{3.2}$$

where S_u is the momentum source, dependent on the cell region as well; P_g is the pressure of the gas phase; $\bar{\bar{\tau}}$ is the stress tensor.

3.1.3 Conservation of Species

The gas phase consists of several gas species whose transport is governed by a general convection-diffusion form as:

$$\frac{\partial}{\partial t}\left(\varepsilon^{\text{eff}} C_i\right) + \nabla \cdot \left(-D_{i,m}^{\text{eff}} \nabla C_i\right) + \nabla \cdot \left(\vec{u}_g C_i\right) = S_i \tag{3.3}$$

where C_i and S_i are the concentration and source term for the ith species, respectively; A_v is the active area per volume ($^1/_m$), which can be calculated as follows [100]: $A_v = \frac{m_{Pt} A_s}{l_c}$; $D_{i,m}^{\text{eff}}$ represents the effective mass diffusion coefficient for species i in the mixture.

3.1.4 Multi-water Phase Transport

There are three phases of water considered in this work. First, water vapor is added to the fuel stream for humidification before entering the gas flow channel. Thus, the transport of water vapor is also governed by the convection-diffusion equation:

$$\frac{\partial}{\partial t}\left(\varepsilon^{\text{eff}} C_v\right) + \nabla \cdot \left(-D_v^{\text{eff}} \nabla C_v\right) + \nabla \cdot \left(\vec{u}_g C_v\right) = S_v \tag{3.4}$$

where C_v is the water vapor concentration, D_v^{eff} is the effective water vapour diffusivity, and S_v is the water vapour source term, which arises from the multi-water phase change processes.

Second, in the polymer electrolyte, water is usually assumed to be in a "dissolved" phase in the electrolyte region. The process is described as:

$$\frac{\partial}{\partial t}(\varepsilon_m C_d) + \nabla \cdot \left(-D_d^{\text{eff}} \nabla C_d\right) + \nabla \cdot \left(\frac{n_d}{F} \vec{J}_m\right) = S_d \tag{3.5}$$

where ε_m is the volume fraction of the polymer membrane ($\varepsilon_m < 1$ in the CL); C_d is the dissolved membrane water concentration; D_d^{eff} is the dissolved water diffusivity in the electrolyte; n_d is the electro-osmotic drag coefficient, $\vec{J}_m$ is the membrane phase current density; S_d is the source term for the dissolved phase.

Finally, the governing equation for the liquid water transport in the gas diffusion and catalyst layers is:

$$\frac{\partial}{\partial t}(\varepsilon \rho_l s) + \nabla \cdot \left(\left(-\frac{\rho_l K_{rl} K}{\mu_l} \frac{dP_c}{ds}\right) \nabla s + \frac{\rho_l \mu_g K_{rl}}{\mu_l K_{rg}} \vec{u}_g\right) = S_l \tag{3.6}$$

where s is the liquid saturation, which is the ratio between liquid volume and void space volume; ρ_l is the volume averaged density; k is the permeability of the porous media; k_{rl} is the relative permeability of the liquid phase; μ_l and P_l are the dynamic viscosity and pressure of the liquid phase, respectively; P_c represents the capillary pressure; μ_g and k_{rg} are the dynamic viscosity and relative permeability of the gas phase, respectively; and S_l is the source term for the liquid water.

3.1.5 Conservation of Energy

The energy equation can be written as:

$$\frac{\partial}{\partial t}\left(\sum_{k=g,s} (\varepsilon \rho E)_k\right) + \nabla \cdot \left(\sum_{j=g,l} (\varepsilon \rho c_P \vec{u})_j T\right) + \nabla \cdot \left(-k^{\text{eff}} \nabla T\right) = S_T \tag{3.7}$$

where k^{eff} is the effective conductivity; S_T contains the heat of chemical reaction, phase change, and any other volumetric heat sources.

3.1.6 Conservation of Charge

The governing equation for the transport of electrons and protons can be expressed as:

$$\nabla \cdot \left(-\sigma_s^{\text{eff}} \nabla V_s\right) = -S_\emptyset \tag{3.8}$$

$$\nabla \cdot \left(-\sigma_m^{\text{eff}} \nabla V_m\right) = S_\emptyset \tag{3.9}$$

where V_s and V_m are the electric potential in the solid phase and electrolyte membrane; σ_s^{eff} and σ_m^{eff} are the electric conductivity of the solid material and membrane, respectively. As mentioned before, carbon monoxide also has electro-oxidation reaction on platinum surface, thus the $S_\emptyset$ in the anode catalyst layer is:

$$S_\emptyset = A_v F\left(q_{H_ox} + 2q_{CO_ox}\right) \tag{3.10}$$

where q_{H_ox} and q_{CO_ox} are electro-oxidation rates of hydrogen and CO, respectively.

3.1.7 Coverage of Species on Anode Catalyst Layer

The steady state assumption is made for the coverage of hydrogen, CO and oxygen:

$$\begin{cases} \xi \frac{\partial \theta_{H_2}}{\partial t} = 2\left(q_{H_ads} - q_{H_des}\right) - q_{H_ox} - 2q_{H-O_ox} \\ \xi \frac{\partial \theta_{CO}}{\partial t} = \left(q_{CO_ads} - q_{CO_des}\right) - q_{CO_ox} - 2q_{CO-O_ox} \\ \xi \frac{\partial \theta_{O_2}}{\partial t} = 2\left(q_{O_ads} - q_{O_des}\right) - q_{H-O_ox} - 2q_{CO-O_ox} \end{cases} \tag{3.11}$$

Bhatia and Wang [93] dropped the middle term on the right hand side of CO coverage balance equation given above, due to the relatively small CO electro-oxidation term compared with other terms. However at lower voltages, because of higher overpotentials at the anode side, CO electro-oxidation becomes non-negligible. Thus, this term is also included in this work. q_{i_ads} are adsorption rates; q_{i_des} are desorption rates; q_{i-O_ox} are heterogeneous oxidation rates. These reaction rates will be obtained through reaction kinetics in the following section. The main physical and operating properties are given in Table 3.1. The source terms used in conservation equations are written in Table 3.2.

Table 3.1 Physical and operating parameters used in model [57, 83, 107]

Parameter (unit)	Value
Platinum mass loading, m_{Pt} (kg/m^2)	0.004
Porosity: GDL/CL, ε_c	0.6/0.3
Mass Ratio, f_{Pt}	0.2
Active area, A_v $(1/m)$	2.19×10^7
Molar area density of platinum catalyst sites, ξ (mol/m^3)	1.55×10^3

Table 3.2 Source terms in conservation equations [7]

	S_m	S_u	S_i	S_l	S_d	$S_\emptyset$	S_T
Channel	0	0	0	0	0	0	0
Electrode	S_v	$-\frac{\mu_g}{K}\vec{u}_g$	$S_v = -\frac{S_{vl}}{M_w}$	S_{vl}	0	0	$\frac{J_s^2}{\sigma_s} + S_{vl}h_{fg}$
ACL	$S_i + S_v$	$-\frac{\mu_g}{K}\vec{u}_g$	$S_i = -A_v q_{i_ads}$ $S_v = -\frac{S_{vl}}{M_w} - S_{vd}$	S_{vl}	S_{vd}	$A_v F(q_{H_ox} + 2q_{CO_ox})$	$\eta_a R_a + \frac{J_s^2}{\sigma_s} + \frac{J_m^2}{\sigma_m} + S_{vl}h_{fg} + M_w S_{vd} h_{m,fg}$
CCL	$S_{O_2} + S_v$	$-\frac{\mu_g}{K}\vec{u}_g$	$S_{O_2} = -\frac{R_c}{4F}$ $S_v = \begin{cases} vp: -\frac{S_{vl}}{M_w} + \frac{R_c}{2F} \\ lp: -\frac{S_{vl}}{M_w} \\ dp: -\frac{S_{vl}}{M_w} \end{cases}$	$\begin{cases} vp: S_{vl} - M_w S_{ld} \\ lp: S_{vl} - M_w S_{ld} + \frac{M_w R_c}{2F} \\ dp: S_{vl} - M_w S_{ld} \end{cases}$	$vp: S_{ld}$ $lp: S_{ld}$ $dp: S_{ld} + \frac{R_c}{2F}$	R_c	$\left(\left\lvert\frac{(T\Delta S)}{4F}\right\rvert + \eta_c\right) R_c + \frac{J_s^2}{\sigma_s} + \frac{J_m^2}{\sigma_m} + S_{vl}h_{fg} + M_w S_{ld}(h_{m,fg} - h_{fg})$
Membrane	0	-10^{30}	0	0	0	0	$\frac{J_m^2}{\sigma_m}$
vp: vapor production; lp: liquid production; dp: dissolved production; $i \equiv H_2, CO, O_2$.							

3.2 Reaction Kinetics

In the presence of carbon monoxide and oxygen in the fuel feed, the reaction kinetics of the hydrogen oxidation reaction (HOR) in the anode catalyst layer is altered. At the low operating temperatures of PEM fuel cells, the sticking probability of CO onto the platinum catalyst is high; hence the anode catalyst layer is said to be poisoned by CO. This phenomenon implies that the reaction sites are available for HOR for drastic reduction to occur, decreasing the overall performance of the cell. The electro-oxidation reaction of hydrogen proceeds—via a Tafel reaction, followed by a Volmer reaction. The Tafel reaction is depicted as the electro-oxidation of hydrogen and requires two adjacent bare platinum sites as given below [12]:

$$H_2 + 2Pt \leftrightarrow 2(H - Pt) \tag{3.12}$$

The Volmer reaction is a discharge step and is expressed as [12]:

$$2(H - Pt) \leftrightarrow 2Pt + 2H^+ + 2e^- \tag{3.13}$$

With carbon monoxide in the fuel stream, the CO molecules adsorb onto the platinum sites according to [97]:

$$CO + Pt \leftrightarrow CO - Pt \tag{3.14}$$

The electro-oxidation of adsorbed CO molecules occurs at high electrode potentials via the "reactant pair" mechanism [97]:

$$CO - Pt + H_2O \leftrightarrow Pt + CO_2 + 2H^+ + 2e^- \tag{3.15}$$

The reaction set given by Equation (3.12-3.15) is the basis of the CO poisoning mechanism [62]. Since the CO-Pt bond is much stronger than that of H-Pt bond, the chemisorptions of CO onto the platinum sites creates an obstacle for the hydrogen electro-oxidation [36]. As stated in [13], the adsorbed CO on platinum surface could only be oxidized until the potential reaches about 0.7 V. Thus, the water consumed in Equation (3.15) has little influence on water management in this model. In addition, since the electro-oxidation of CO requires high anode over-potential, its removal via electro-oxidation is difficult. Hence, oxygen is usually fed to the anode side to mitigate the effects of CO poisoning. This mechanism is referred to as oxygen bleeding and was introduced by Gottesfeld and Pafford [59]. Oxygen in the fuel stream allows for the heterogeneous oxidation of CO by reacting with the carbon monoxide adsorbed onto the platinum sites. At low operating temperatures, the gas phase oxidation of carbon monoxide and hydrogen by oxygen is assumed to be negligible and the oxidation is mainly through the heterogeneous catalysis [36]. Chemically, the heterogeneous oxidation of CO on platinum is described by a Langmuir-Hinshelwood mechanism [98]:

$$CO + Pt \leftrightarrow CO - Pt \tag{3.16}$$

$$O_2 + 2Pt \leftrightarrow O_2 - Pt + Pt \rightarrow 2(O - Pt) \tag{3.17}$$

$$CO - Pt + O - Pt \rightarrow CO_2 + 2Pt \tag{3.18}$$

The oxygen also reacts with the adsorbed hydrogen. The heterogeneous oxidation of hydrogen by oxygen is also approximated by a Langmuir-Hinshelwood mechanism [99]. Also, the water produced through Equation (3.21) could also be ignored due to the small amount of oxygen introduced to the anode channel.

$$H_2 + 2Pt \leftrightarrow 2(H - Pt) \tag{3.19}$$

$$O_2 + 2Pt \leftrightarrow O_2 - Pt + Pt \rightarrow 2(O - Pt) \tag{3.20}$$

$$O - Pt + 2(H - Pt) \rightarrow H_2O + 3Pt \tag{3.21}$$

3.2.1 Hydrogen Reaction Rate

The adsorption and desorption rates of hydrogen depending on Langmuir Kinetics are given in Equation (3.22) and Equation (3.23), in which the surface adsorption rate constant is independent of surface coverage [96]. The hydrogen electro-oxidation rate is described by the Butler-Volmer equation. In this study, the charge transfer coefficient, α, is assumed to be 0.5; hence, the Butler-Volmer equation would be simplified to a hyperbolic sine term as Equation (3.24).

$$q_{H_ads} = K_{H_ads} C_{H_2} (\Theta_{Pt})^2 \tag{3.22}$$

$$q_{H_des} = B_{H_des} K_{H_ads} C_{H_2} (\Theta_H)^2 \tag{3.23}$$

$$q_{H_ox} = 2K_{H_ox} \Theta_H \sinh\left(\frac{F\eta_a}{2RT}\right) \tag{3.24}$$

where K_{H_ads} is the rate constant of hydrogen adsorption which is independent of its surface coverage, B_{H_des} is the rate constant of hydrogen desorption, C_{H_2} is the concentration of hydrogen. K_{H_ox} is the rate constant of hydrogen oxidation and η_a is the anode overpotential.

3.2.2 Carbon Monoxide Reaction Rate

The adsorption and desorption rates of carbon monoxide are based on Temkin kinetics follows in Equation (3.25) and Equation (3.26), which is modeled as a function of the surface coverage of adsorbed species [96]; while the reaction rate of carbon monoxide could also be simplified by the Butler-Volmer equation as given by Equation (3.27).

$$q_{CO_ads} = K_{CO_ads} C_{CO} (\theta_{Pt}) exp\left(\frac{-\beta r \theta_{CO}}{RT}\right) \tag{3.25}$$

$$q_{CO_des} = B_{CO_des} K_{CO_ads} \theta_{CO} exp\left(\frac{-[1-\beta] r \theta_{CO}}{RT}\right) \tag{3.26}$$

$$q_{CO_ox} = 2K_{CO_ox}\theta_{CO}\sinh\left(\frac{F\eta_a}{2RT}\right) \tag{3.27}$$

where K_{CO_ads} and B_{CO_des} are the rate of adsorption and desportion of carbon monoxide, respectively, β is a symmetry factor, 0.05 is used here, and r is an interaction parameter depending on the temperature [101], because the temperature cannot exceed 373 K for the conventional PEM fuel cell, thus r is assumed to be a constant as 39.7 KJ/mol here. K_{CO_ox} is the rate of the electro-oxidation of carbon monoxide.

3.2.3 Oxygen Reaction Rate

The rates of oxygen adsorption and desorption are given in Equation (3.28) and Equation (3.29), respectively. Moreover, the heterogeneous oxidation rates of adsorbed hydrogen and carbon monoxide are given by Equations (3.30) and (3.31), respectively [102].

$$q_{O_ads} = K_{O_ads}C_{O_2}(1 - \theta_H - \theta_{CO} - \theta_O)^2 \tag{3.28}$$

$$q_{O_des} = B_{O_des}K_{O_ads}(\theta_O)^2 \tag{3.29}$$

$$q_{H-O_ox} = K_{H-O_ox}\theta_O(\theta_H)^2 \tag{3.30}$$

$$q_{CO-O_ox} = K_{CO-O_ox}\theta_O\theta_{CO} \tag{3.31}$$

where K_{O_ads} and B_{O_des} are the rates of adsorption and desorption of oxygen. K_{H-O_ox} and K_{CO-O_ox} are the rates of the heterogeneous oxidation of hydrogen and carbon monoxide, respectively.

The reaction rate constants are expressed in terms of Arrhenius law as follows [57]:

$$K_i = K_i^0 exp\left(\frac{-E_i^K}{RT}\right) \tag{3.32}$$

$$B_i = B_i^0 exp\left(\frac{-E_i^b}{RT}\right) \tag{3.33}$$

where the pre-exponential constants, $K_i^0$and B_i^0, and the activation energy, E_i^K and E_i^b, are given in Table 3.3.

Table 3.3 Kinetic parameters used in this model [103]

Parameters (units)	Value	Parameters (units)	Value
$K^0_{H_ads}$ $(c/mol.s)$	1.30×10^{10}	$K^0_{CO_ox}(c/m^3.s))$	3.79×10^{17}
$E^k_{H_ads}$ (kJ/mol)	10.4	$E^k_{CO_ox}$ (kJ/mol)	127
$K^0_{H_ox}$ $(c/m^3.s)$	4.62×10^{7}	$K^0_{O_ads}$ $(c/mol.s)$	1.39×10^{8}
$E^k_{H_ox}$ (kJ/mol)	16.7	$E^k_{O_ads}$ (kJ/mol)	14.2
$B^0_{H_des}$ (mol/m^3)	1.99×10^{-3}	$B^0_{O_des}$ (mol/m^3)	3.57×10^{20}
$E^b_{H_des}$ (kJ/mol)	87.9	$E^b_{O_ads}$ (kJ/mol)	250
$K^0_{CO_ads}$ $(c/mol.s)$	1.82×10^{15}	$K^0_{H-O_ox}$ $(c/m^3.s)$	1.57×10^{13}
$E^k_{CO_ads}$ (kJ/mol)	47.3	$E^k_{H-O_ox}$ (kJ/mol)	65.9
$B^0_{CO_des}$ (mol/m^3)	8.55×10^{-5}	$K^0_{CO-O_ox}$ $(c/m^3.s)$	5.59×10^{15}
$E^b_{CO_ads}$ (kJ/mol)	100	$E^k_{CO-O_ox}$ (kJ/mol)	90

The values for parameters used in literature are shown in Table 3.4 and Table 3.5. The parameters in models [40, 54, 93] are all assumed to be constant, which are actually changing depending on their activation energy. In addition, K_{H_ads} and B_{CO_des} should be functions of CO coverage [93], which is also ignored in those models. Moreover, the parameters used in the present work are based on those used in a 2D model [57], which are decided by pre-exponential constants and activation energy. All activation energy are the same as in [57], while the pre-exponential constants of reactions are changed a little when the values are transferred to 3D. The parameters are still in the range of variability [62]. The modeling results are compared with experimental data favorably, which will be shown in Chapter 5 and Chapter 6.

Table 3.4 Kinetic parameters in former models [40, 54, 93]

Parameters (units)	Value [40]	Value [54]	Value [93]
$K_{H_ads}(A/m^2.atm)$	4×10^4	4×10^7	1×10^6
$B_{H_des}(atm)$	0.5	0.5	0.5
$K_{CO_ads}(A/m^2.atm)$	2.4×10^5	1×10^5	1×10^5
$B_{CO_des}(atm)$	2×10^{-5}	1.51×10^{-8}	2.75×10^{-7}
$K_{H_ox}(A/m^2)$	5×10^3	4×10^4	–
$K_{CO_ox}(A/m^2)$	10^{-2}	1×10^{-8}	–

Table 3.5 Kinetic parameters in former models [57]

Parameters (units)	Value	Parameters (units)	Value
$K^0_{H_ads}\ (m/s)$	298	$K^0_{CO_ox}(mol/m^2.s)$	3.40×10^{10}
$E^k_{H_ads}\ (kJ/mol)$	10.4	$E^k_{CO_ox}\ (kJ/mol)$	127
$K^0_{H_ox}\ (mol/m^2.s)$	231	$K^0_{O_ads}\ (m/s)$	2.0
$E^k_{H_ox}\ (kJ/mol)$	16.7	$E^k_{O_ads}\ (kJ/mol)$	14.2
$B^0_{H_des}\ (mol/m^3)$	4.18×10^{11}	$B^0_{O_des}\ (mol/m^3)$	1.36×10^{36}
$E^b_{H_des}\ (kJ/mol)$	87.9	$E^b_{O_ads}\ (kJ/mol)$	250
$K^0_{CO_ads}\ (m/s)$	2×10^5	$K^0_{H-O_ox}\ (mol/m^2.s)$	3.28×10^4
$E^k_{CO_ads}\ (kJ/mol)$	47.3	$E^k_{H-O_ox}\ (kJ/mol)$	65.9
$B^0_{CO_des}\ (mol/m^3)$	6.87×10^2	$K^0_{CO-O_ox}\ (mol/m^2.s)$	5.0×10^8
$E^b_{CO_ads}\ (kJ/mol)$	100	$E^k_{CO-O_ox}\ (kJ/mol)$	90.0

3.3 Boundary and Initial Conditions

The governing equations (3.1-3.11) are solved in a single computational domain as shown in Figure 3.1. Thus, boundary conditions are needed to be specified on the outer surfaces of the domain. The temperature at the inlet boundaries is set to 358 K. Meanwhile, at the flow inlet boundaries, liquid

saturation is fixed to s=0, and the inlet concentrations of gases on the anode side and oxygen on the cathode side, can be specified as follows, based on the temperature, pressure, and relative humidity at the anode and cathode inlets.

$$C_{CO} = CO_{in}\frac{P_a}{RT_0} \tag{3.34}$$

$$C_{O_2_a} = O_{2in_a}\frac{P_a}{RT_0} \tag{3.35}$$

$$C_{H_2} = \frac{P_a\left(1-CO_{in}-O_{2in_a}\right)-RH_aP^{sat}}{RT_0} \tag{3.36}$$

$$C_{O_2_c} = \frac{0.21\left(P_c-RH_cP^{sat}\right)}{RT_0} \tag{3.37}$$

where P_a and P_c are the inlet gas pressure at the anode and cathode, respectively; T_0 is the inlet gas temperature; CO_{in} and O_{2in_a} are the molar concentration of carbon monoxide and oxygen in the fuel stream at the anode inlet; RH_a and RH_c are the inlet relative humidity of the anode and cathode gas streams at the each inlet.

At the flow outlet, fully developed boundary condition is applied so that there are no variations of fluxes for all variables in the normal direction. Furthermore, the operating pressure is specified at the gas channel outlet and the operating temperature is specified on the channel walls.

The solid phase potential, $V_{s,c}$, is fixed at zero at the bipolar plate and cathode electrode interface; then the solid phase potential at the interface between the anode electrode and the anode bipolar plate, $V_{s,a}$, is given as the overall potential loss across the whole cell, namely:

$$V_{s,a} = \eta_{cell} = V_{rec} - V_{cell} \tag{3.38}$$

The reversible cell voltage is calculated from the Nernst equation as follows:

$$V_{rec} = \frac{\Delta G^{ref}}{2F} + \frac{\Delta S^{ref}}{2F}\left(T - T^{ref}\right) + \frac{RT}{2F}ln\left[\left(\frac{P_{H_2}}{P^{ref}}\right)\left(\frac{P_{CO}}{P^{ref}}\right)\left(\frac{P_{O_2_a}}{P^{ref}}\right)^{1/2}\left(\frac{P_{O_2_c}}{P^{ref}}\right)^{1/2}\right] \tag{3.39}$$

where, ΔG^{ref} is the Gibbs free energy change; ΔS^{ref} is the entropy change for the overall reaction; T^{ref} and P^{ref} are the reference temperature and pressure, respectively; P_{H_2}, P_{CO}, and $P_{O_2_a}$ are species partial pressures in the anode fuel stream, while $P_{O_2_c}$ is the oxygen partial pressure in the cathode side.

The second term of Equation (3.39) stands for the effect of temperature, while the last term represents the effect of the partial pressure and reactant concentration on the reversible cell potential.

In addition, the anode overpotential is defined as the difference between the solid phase and membrane phase potentials:

$$\eta_a = V_s - V_m \tag{3.40}$$

The initial conditions for transient modeling are either zero or steady-state field from a previous operating point. Finally, for the remaining boundary conditions not specifically mentioned here, a specific form of a Neumann condition applies (no flux or symmetry condition):

$$\frac{\partial \Theta}{\partial n} = 0 \tag{3.41}$$

where Θ can be any variables of interest.

Chapter 4
Numerical Implementation

4.1 Numerical Procedure

The present simulation involves 3D multi-phase transport of species, energy, momentum and charged species with the 3D domain of a single PEM fuel cell as shown in Figure 3.1. The structure in this study is based on the work done by Wu [7] with a non-uniform grid scheme by using pre-processing software, GAMBIT 2.3. The solution is implemented in the commercial software package Fluent (6.3.26). The governing equations (3.1-3.11) are discretized by a second-order upwind scheme and solved with a finite volume method. Moreover, various source terms, model parameters, empirical correlations, material properties, and boundary conditions were coded using the programming language C in terms of the user defined functions (UDF). Three more user-defined scalar (UDS) equations have been added into this work, they are about the coverage of hydrogen, CO, and oxygen in anode catalyst layer, respectively. Worth to point out that each term of the UDS equation of CO coverage is enlarged by 3-orders to increase its sensitivity when it is at a steady state, since the numerical results of these terms are too small to get the accurate data. In addition, some controlling strategies and under-relaxation schemes were also developed with UDFs. In order to result in a faster convergence, the under-relaxation factors for species sorption rates, reaction rates and coverage are set to be 0.9 for each term. However, the under-relaxation factors of the outer loop which couples CO coverage and oxygen coverage with former equations are set to be 0.1 at the beginning for system instability; then these factors could be increased to 0.99 after a certain level of stabilization to speed up the convergence. When steady state flow is applied, the SIMPLE algorithm is selected for the coupling between the pressure and velocity field. In addition, an algebraic multi-grid (AMG) method with a Gauss-Seidel type smoother is used to accelerate the convergence. A strict convergence criterion with a residue of 10^{-6} was used for the computation of all the variables. Generally, the criterion with a residue of 10^{-3} is sufficient for most of the situations. Meanwhile, when transient flow is applied, an adaptive time stepping algorithm is adopted, which is able to automatically determine the time step as the calculation proceeds with a minimum of 10^{-4} s and a maximum of 10 s time step sizes. Last but not least, because the input of CO is extremely small in units of parts per million, the under-relaxation and linearization techniques are required to solve this problem.

4.2 Grid Independent Solution

A grid independency test for the current grid system has been illustrated in [83] in details. The grid size could be extremely small to get an accurate result; on the other hand, smaller grid size will lead to a longer time for computation. In a 3D numerical model, the number of grid points is only varied in one direction while the numbers along the other directions are fixed. Take y direction as an example, changing N^y when N^x and N^z are set as constant. The system will diverge when N^y is less than 5 or more than 25. Therefore, N^y=25 is considered as the "exact solution". However, more grid points will result in a longer computational time. N^y is selected as 15 in this model. Finally, the number of non-uniform grid points in each direction (N^x, N^y, and N^z) is optimized to (20, 15, 50). The corresponding solution errors are (0.49%, 1.88%, and 0.009%), respectively in each of the directions, which are calculated using:

$$Err = \left|\frac{\Theta' - \Theta}{\Theta'}\right| \times 100\% \tag{4.1}$$

where Θ' is the solution and Θ represents the variables to be compared.

Thus, the total error for the final mesh is roughly estimated as:

$$Err \leq \sqrt{|Err^x|^2 + |Err^y|^2 + |Err^z|^2} = 1.94\% \tag{4.2}$$

Chapter 5
Results and Discussion – Part I: Steady State

5.1 Validation of Steady State Model

In the present numerical study, several input parameters are set for different conditions. They are cell voltage V_{cell}, inlet gas pressure P_a, P_c, gas relative humidities RH_a, RH_c, and stoichiometric ratios ξ_a, ξ_c.

In the base study, the cell output voltage is set to 0.55 V; the inlet gas pressure is 101 kPa; gas humidity is 100% in both channel inlets; and the stoichiometric ratios are 1.2 and 2.0 for the anode and cathode stream, respectively. In addition, the operating temperature is a constant of 358 K at the inlet. The data used in the 1D figures are volume average values. Moreover, most 3D results in this thesis are focused on anode catalyst layer, since the poisoning reactions are reacting on platinum, except that the multi-phase water transport may happen in membrane and cathode side as well.

In this model, the numerical results of a cell running on pure hydrogen and a fuel mixture containing CO fit to the experimental data well, as shown in Figure 5.1.

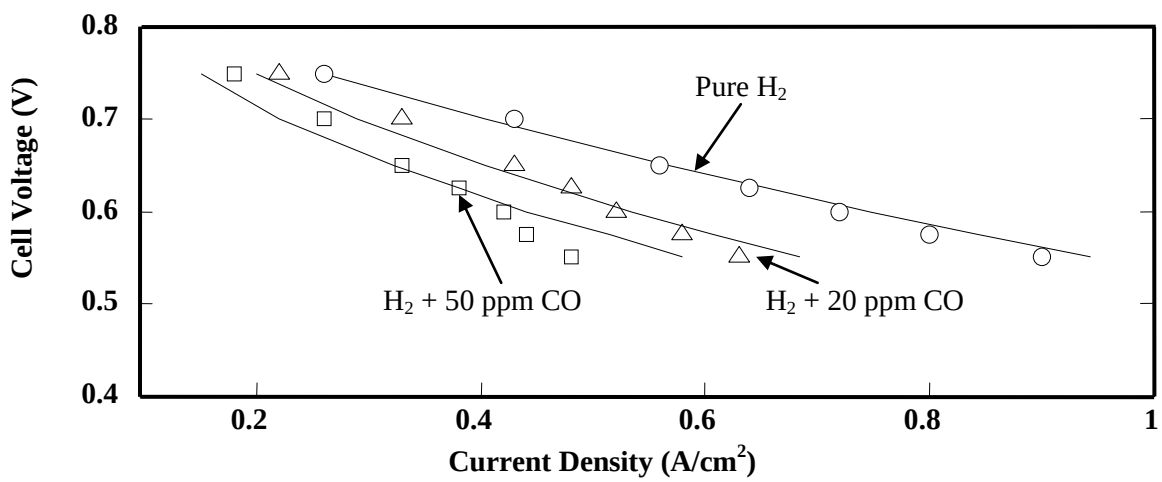

Figure 5.1 Comparison of the cell performance predictions with the experimental results. The points represent actual experimental results [105], and the curves represent simulations based on the model developed.

5.2 Effect of CO Concentration on Fuel Cell Performance

Due to highly preferential adsorption of CO compared with hydrogen, it is noted that the introduction of small amounts of CO into the fuel stream will result in the significant degradation of the cell performance in Figure 5.1. When pure hydrogen is supplied, the current density could almost reach 1.0 A/cm^2; while the maximum current density could only be 0.5 ~ 0.6 A/cm^2 when the anode fuel is contaminated with 50 ppm CO. It also shows that the current density drops very quickly when the cell voltage is increasing at a large amount of CO contaminant. In addition, the performance degradation is especially highlighted at high current densities, which is due to the adsorption of hydrogen to produce high current density requires more active catalyst surface area, while the production of low current density does not need much catalyst area for hydrogen adsorption. The significant variation also happens to anode overpotential as shown in Figure 5.2. Since, in order to compensate the CO covered catalyst layer surface, it needs more activation push, so the anode kinetic loss increases as the content of CO in the fuel stream increases.

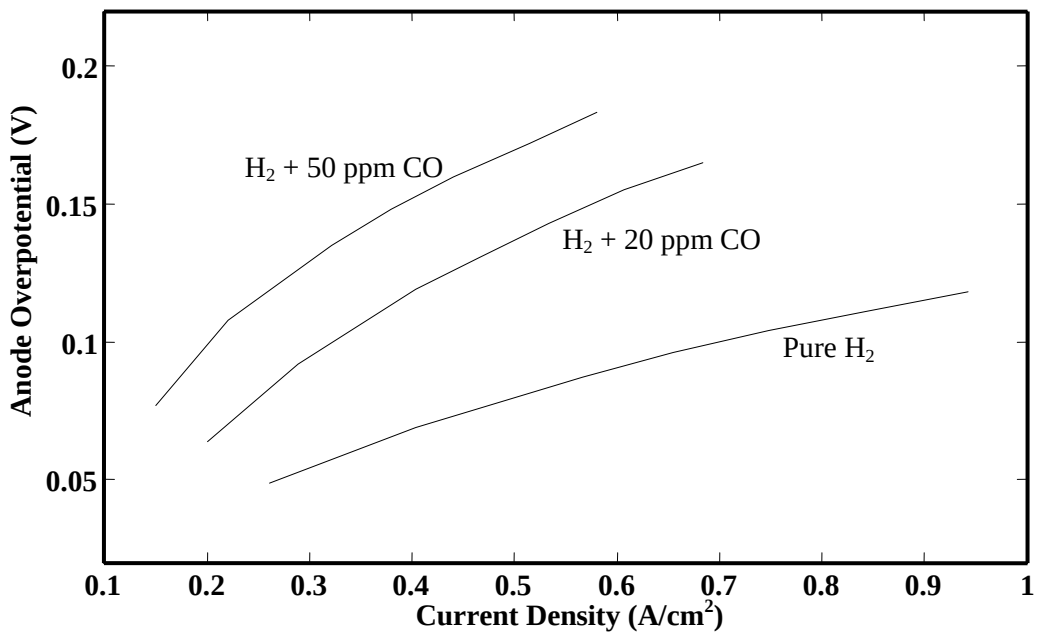

Figure 5.2 Model predictions of anode overpotential changing with current density

Moreover, the coverage of each species is presented in Figure 5.3. It shows that the coverage of hydrogen on the platinum surface decreases from 0.823 to 0.125, while the coverage of CO on the platinum surface increases from 0 to 0.762. The third line stands for the void area of platinum without sticking any gases, which doesn't change a lot at a steady state. It is obviously seen that the slope of coverage is much steeper at lower CO content, and the watershed is about 20 ppm CO in this case. The phenomenon shows us that the catalyst surface becomes saturated at a critical level of CO. Consequently, the fuel cell performance will be degraded significantly even with a small amount of CO, which shows its sensibility to CO poisoning; however, the degradation will come to a slight increase as a result of the CO poisoning saturation.

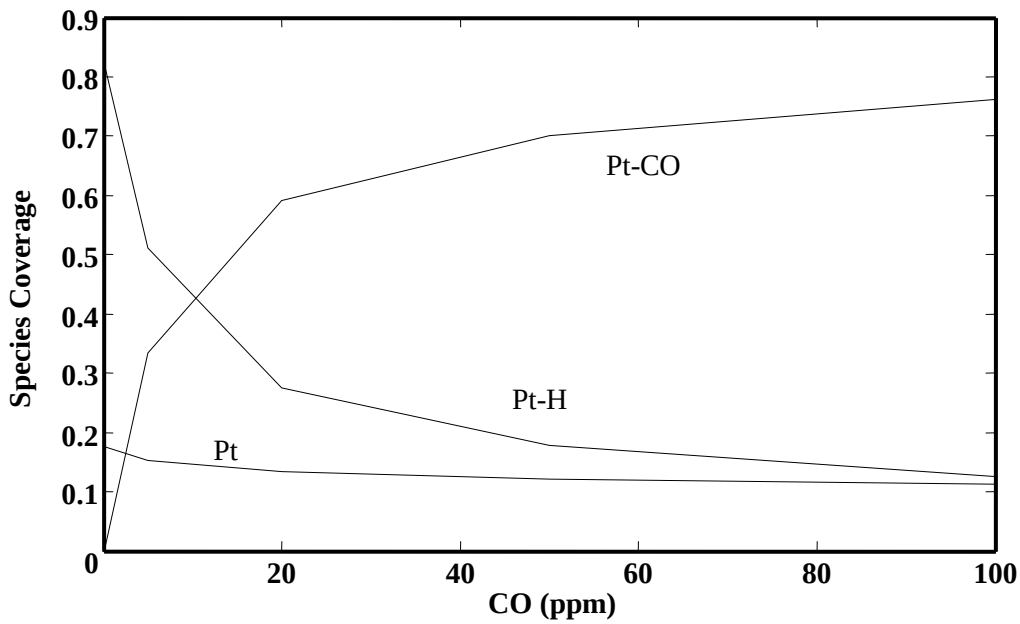

Figure 5.3 Model predictions of species' coverage on anode catalyst layer changing with CO concentration

As mentioned above, the performance degradation is highlighted at high current densities. It could be explained by the interesting finding for coverage of species. Because the increment of current density will result in a higher Pt-CO coverage as well as a lower Pt-H coverage as shown in Figure 5.4, which leads to a more severe degradation of cell performance, with a certain amount of CO contamination.

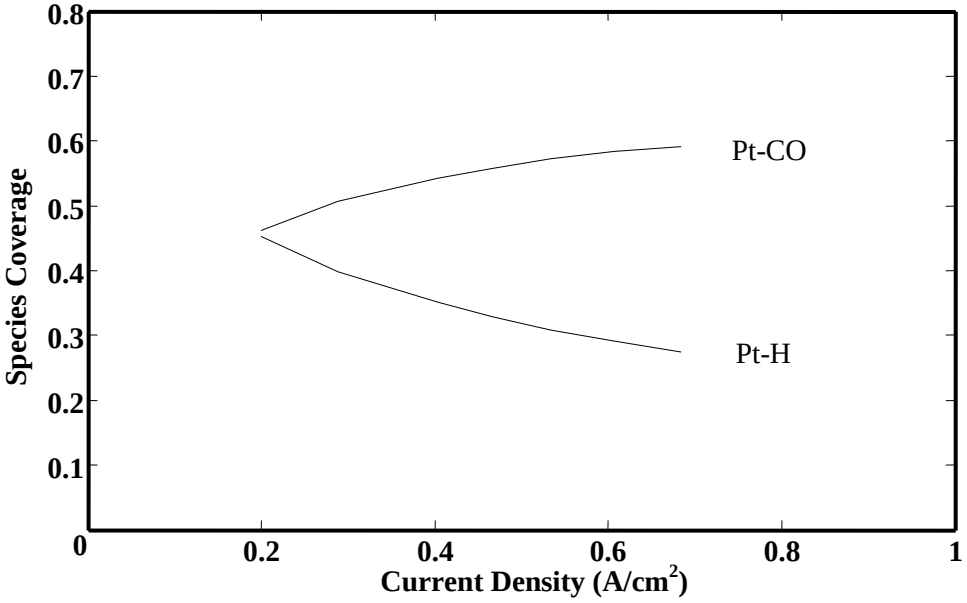

Figure 5.4 Model predictions of species' coverage on anode catalyst layer changing with current density when 20 ppm CO is added into anode fuel feed

5.3 Effect of CO Poisoning in 3D Distribution

After the analysis of the effect of CO concentration on fuel cell performance, there are more detailed three dimensional figures about species' concentration, coverage, sorption/reaction rates in anode catalyst layer illustrated below, which can help us to understand the underlying electrochemical reaction kinetics and poisoning phenomena better.

Firstly, it is clearly seen that the concentrations of hydrogen and CO increase along the channel in Figure 5.5, which is counter-intuitive in the sense that the species' concentrations should decrease down the channel due to the consumption of fuel. This may be explained by the faster consumption of water vapor than that of hydrogen and CO in the anode channel, so that the concentration of hydrogen and CO will increase correspondingly in the fully humidified case.

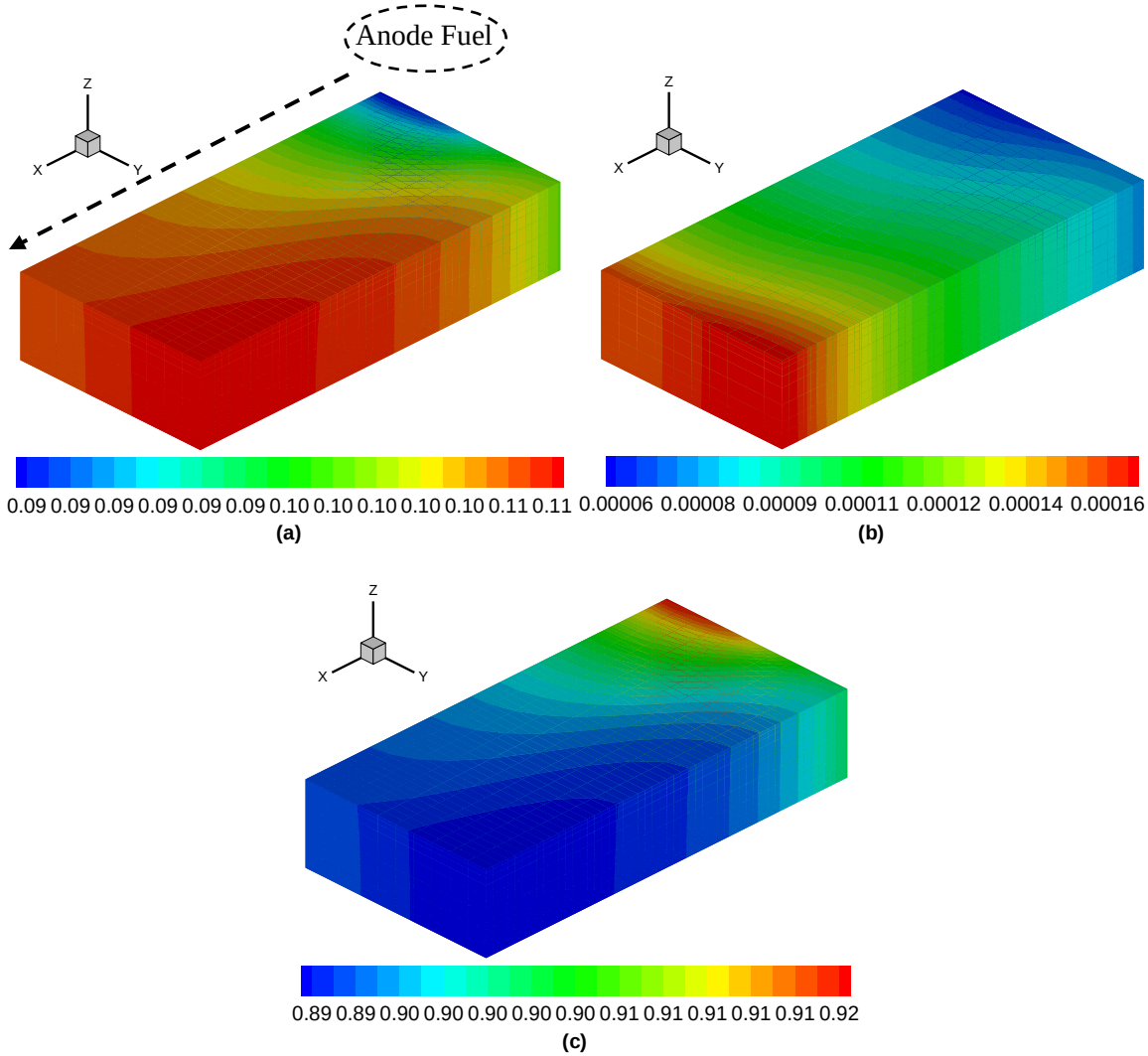

Figure 5.5 (a) Mass fraction of hydrogen; (b) Mass fraction of CO; (c) Mass fraction of H_2O. (Mass fraction distributions in anode catalyst layer when anode fuel is contaminated by 20 ppm CO)

Another interesting phenomenon is found in the pure hydrogen case: the coverage of hydrogen is increasing along the channel as a result of the increment of its mass concentration as shown in Figure 5.6 (a). However, in the case of mixture fuel feed with 20 ppm CO contaminant, the coverage of hydrogen is decreasing along the channel which conflicts with the previous hypothesis. Since in the anode catalyst layer, CO is playing a dominant role of consuming platinum surface area, the decline of hydrogen coverage is caused by the increased CO contaminant, resulting from the increasing CO mass fraction down the channel.

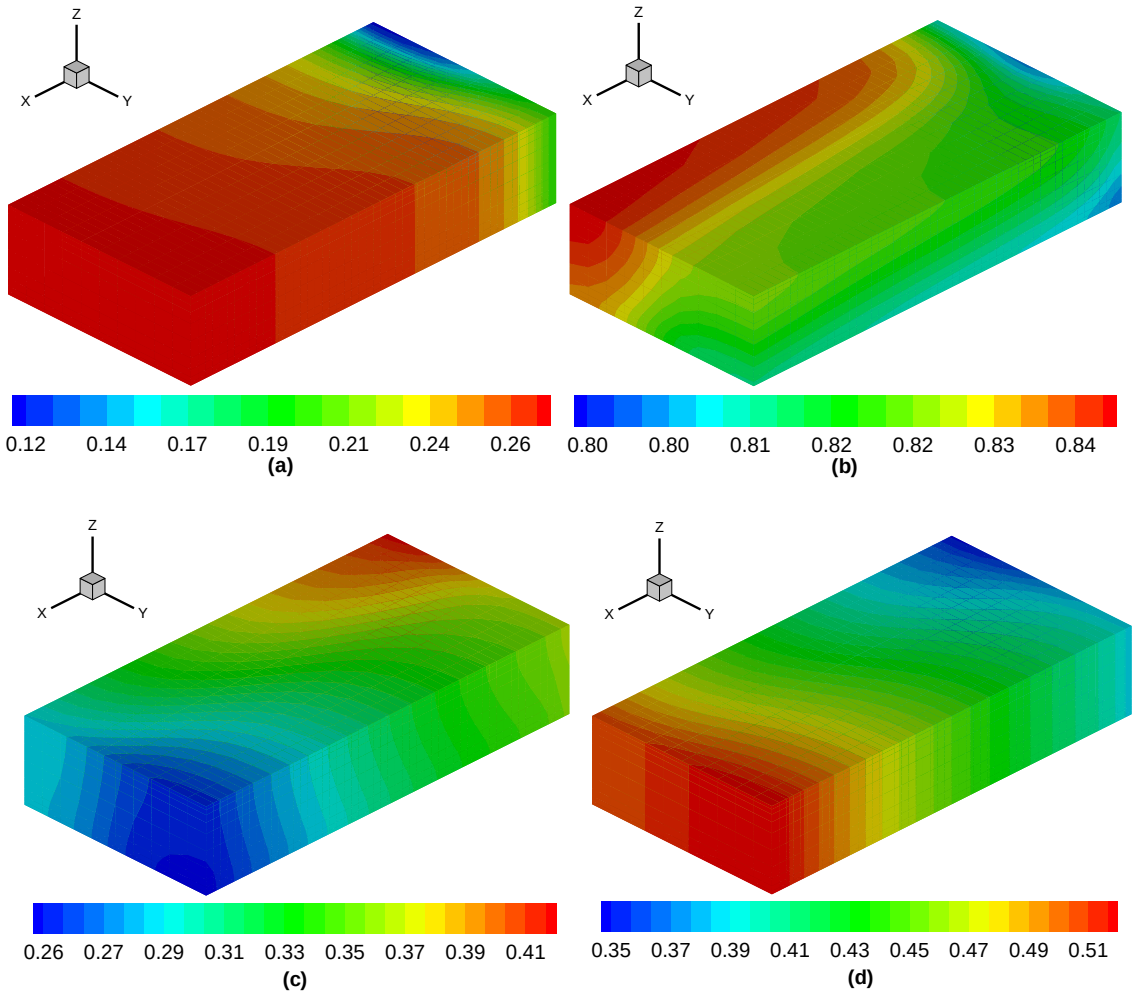

Figure 5.6 (a) Mass fraction of hydrogen with pure hydrogen; (b) Coverage of hydrogen with pure hydrogen; (c) Coverage of hydrogen with 20 ppm CO; (d) Coverage of CO with 20 ppm CO. (Distribution in anode catalyst layer)

After the analysis of species' concentration and coverage, the adsorption rates and electro-oxidation rates are examined. In Figure 5.7, 3D contours about adsorption rate of hydrogen are analyzed with different level of CO poisoning. It is obviously seen that the adsorption rate of hydrogen dropped by $1\sim2\times10^{8}$ with the first 50 ppm CO contaminant. However, referring to Figure 5.7 (c) and (d), extra 50 ppm CO added to the fuel does not make much influence on the adsorption rate of hydrogen, which is fit for the prediction of CO poisoning saturation. In addition, the 3D contours show the adsorption rates of hydrogen are decreasing from the inlet to outlet except that there is little change along the channel with

pure hydrogen. Meanwhile, the adsorption rate is greater over the land area than over the channel. Since the adsorption rate of hydrogen is the function of hydrogen concentration and the avoid surface of catalyst layer as shown in Equation (3.22), so the void space is decreasing along the flow injected direction which is in the second order term will result in a greater influence on hydrogen adsorption rate than the concentration term.

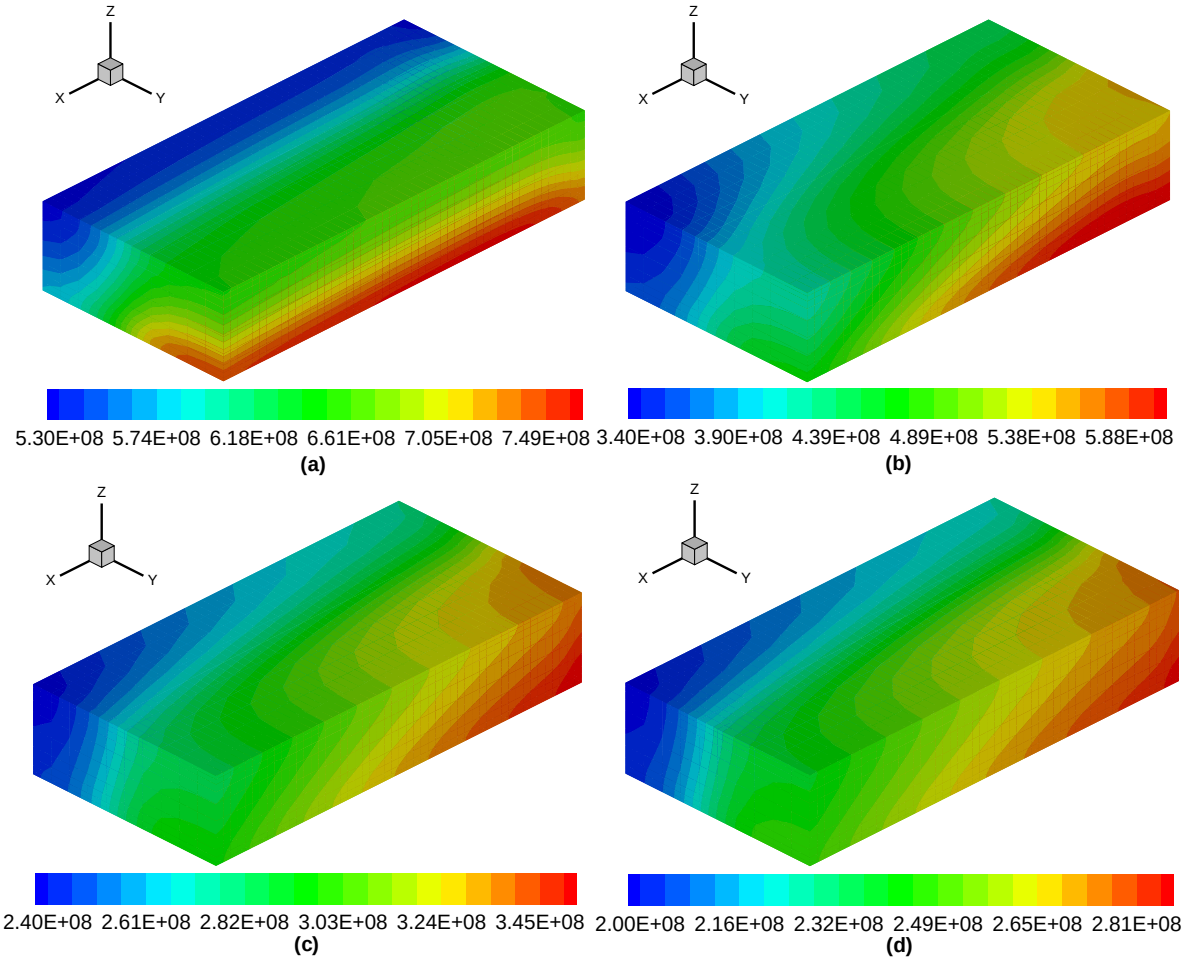

Figure 5.7 Adsorption rate (c/m^3.s) of hydrogen in anode catalyst layer with CO contaminants in the anode fuel gas stream (a) 0 ppm; (b) 5 ppm; (c) 50 ppm; (d) 100 ppm.

Nevertheless, the distribution of adsorption rate of CO is much more complicated than that of hydrogen, as depicted in Figure 5.8, because the CO adsorption rate follows Temkin kinetics which has

an exponential term with its coverage in Equation (3.25). It is interesting to find out that the adsorption rate of CO is decreasing with increasing amount of CO due to the negative exponential term. However, when 100 ppm CO is added in, the distribution of its adsorption rate is different due to the increment of CO concentration is greater than both the decrease of avoid catalyst surface and the exponential term at outlet of land area. At the same time, the 3D figure of CO adsorption rate explains the CO saturation phenomenon very well; it obviously shows that the platinum adsorbs CO very quickly at low CO feed, while the increment of adsorption rate is mitigated at high CO concentration.

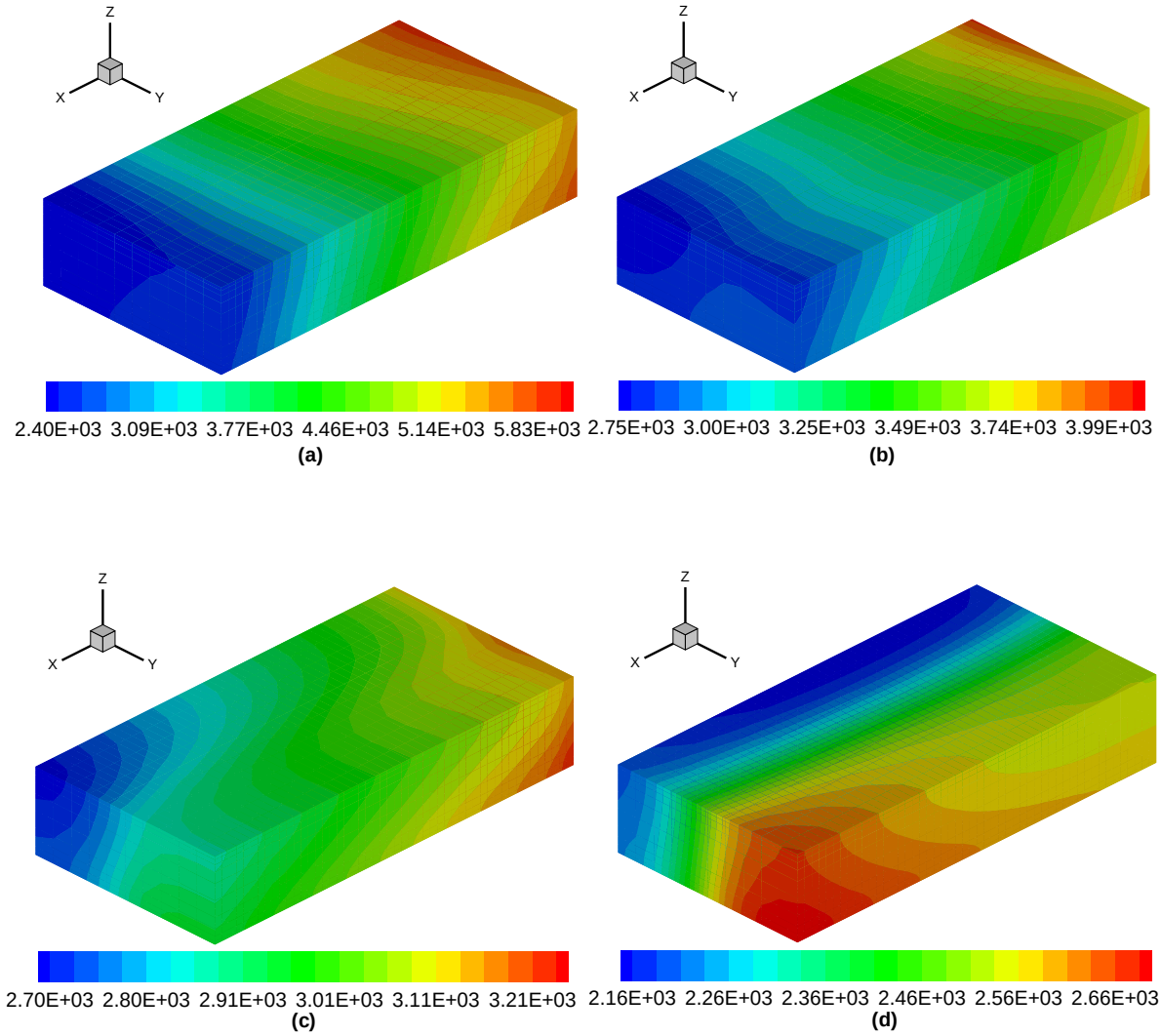

Figure 5.8 Adsoprtion rate (c/m^3.s) of CO in anode catalyst layer with CO contaminants in the anode fuel gas stream (a) 5 ppm; (b) 20 ppm; (c) 50 ppm; (d) 100 ppm.

In addition, compared with Figure 5.7 and Figure 5.8, it is obviously seen that the adsorption rate of CO is about four-orders less than that of hydrogen. But the high adsorption rate of hydrogen does not result in a predominant role in grabbing platinum surface. Because at transient state, the desorption rate of CO is much smaller than its adsorption rate, which means there is little CO will be freed up once they have stuck to the platinum. It is the difference between adsorption, desorption, and reaction rates that motivate the poisoning process to move forward. More detailed explanation is continued in Chapter 6. After the consideration of adsorption rates of species, the reaction rates are also studied as following.

The electro-oxidation rates of hydrogen and CO are depending on their own coverage and anode overpotential. Figure 5.9 shows the electro-oxidation rate of hydrogen is decreasing down the flow channel, while electro-oxidation rate of CO is higher at the outlet than at the inlet. In addition, since the activation overpotential appears in the exponential term has a predominant impact on electro-oxidation rate [105]. Hence, CO poisoning effect is increasing along the flow channel due to the slight decrease of hydrogen electro-oxidation, leading to a lower current density. Besides, the increment of CO electro-oxidation could be ignored compared with hydrogen electro-oxidation rate which is six-orders larger. Hence, the heat generated by the chemical reaction is dominated by the reaction of adsorbed hydrogen, which results in the decline of temperature from inlet to outlet. However, due to the slow chemical reaction of hydrogen in anode catalyst layer which is poisoned by CO impurity, the change of the temperature is not significant except for the inlet.

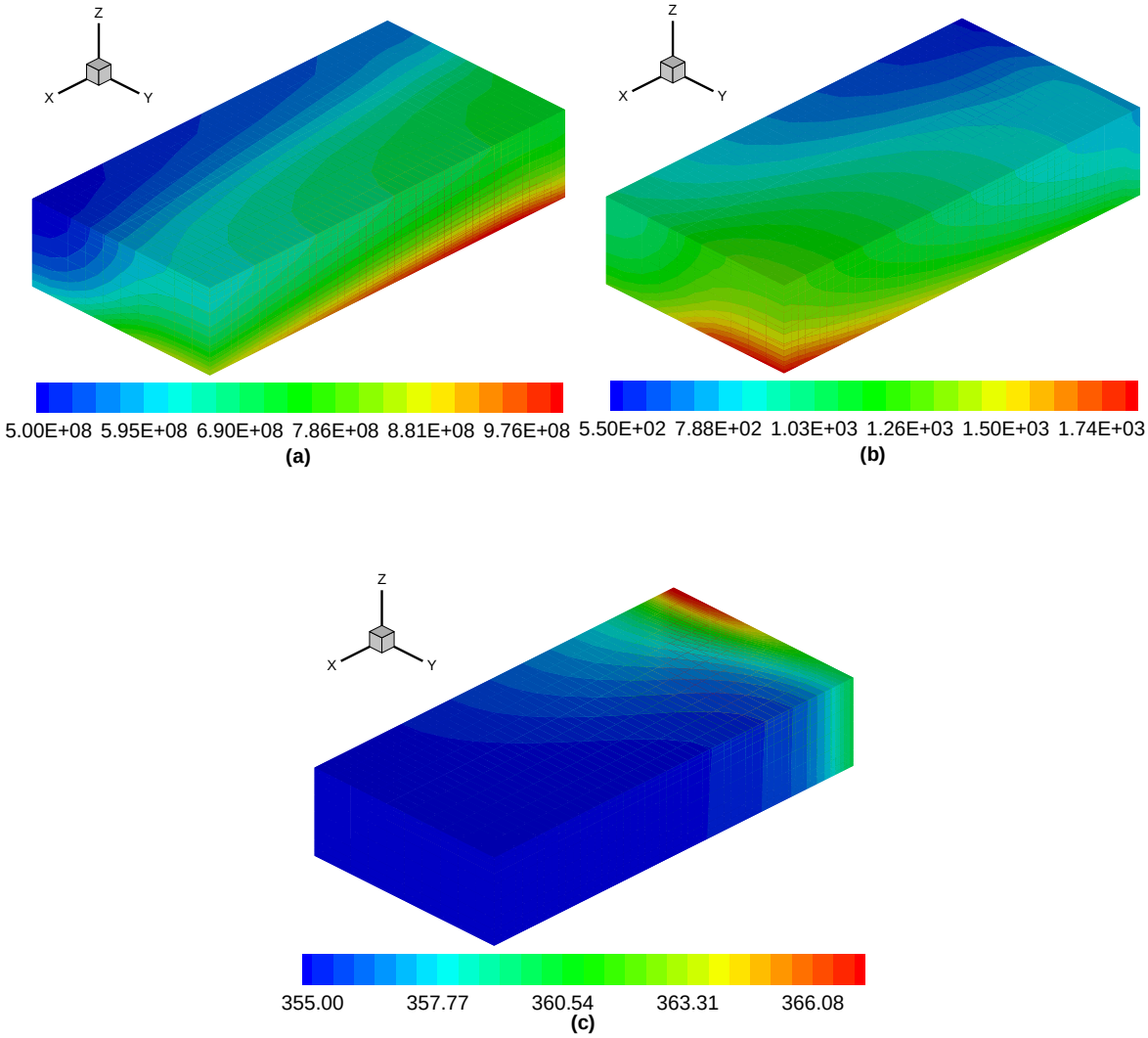

Figure 5.9 (a) Reaction rate (c/m^3.s) of hydrogen; (b) Reaction rate of CO; (c) Temperature distribution. (with 20 ppm CO, the contour is on anode catalyst layer)

The distribution of anode overpotential as shown in Figure 5.10 helps understand many phenomena that occur simultaneously inside of fuel cell better. Because the coverage of hydrogen is much higher over the channel than over the land area, as well as the inlet has adsorbed more hydrogen over outlet, which means it is short in hydrogen supply on the land area and at the outlet site compared with over channel and at the inlet site. Thus more anode overpotential is needed to drive the activation of fuel on these sites. Figure 5.10 also shows that the overpotential increases from the electrode to the membrane, depending on the

species coverage. In short, it is interesting to find out that all variables have internal relationships with each other directly or indirectly.

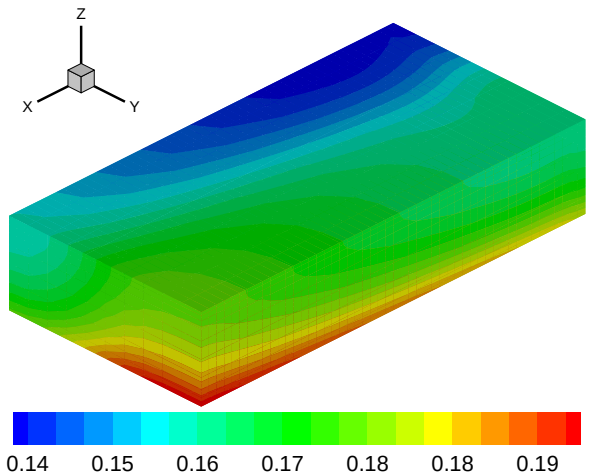

Figure 5.10 Distribution of anode overpotential (V). (with 20 ppm CO, the contour is on anode catalyst layer)

5.4 Effect of Oxygen Bleeding

Since the oxygen bleeding is considered as the most effective mitigation method for CO poisoning presently; in order to understand the effects better, the mitigation process via oxygen bleeding is analyzed in this part. Figure 5.11 shows the fuel cell performance is recovering due to the introduction of oxygen in anode fuel feed. The oxygen added into anode fuel can lead to the heterogeneous oxidation of CO occurring in the anode catalyst layer. At the same time, the local concentration of CO is lowered after oxygen is added in. Hence, the combined effects of lowering CO concentration and the heterogeneous oxidation along the channel will result in an extremely recovery effect. In addition, the quanta of oxygen used in this case fall within the safety range.

The great influence of oxygen bleeding has been demonstrated in many works already; however, little work has been done to penetrate into the real distribution of oxygen bleeding in the anode catalyst layer. Figure 5.11 is based on the case with 100 ppm CO contaminant, which shows that the current density increase significantly once oxygen is added into anode fuel stream; however, the recovery of cell performance is becoming slow after the percentage of oxygen is over 0.5%. Therefore, more oxygen added over 0.5% (molar concentration) will be a waste in this case. However, an incompatible question

comes up; in that the heterogeneous oxidation of hydrogen by oxygen will consume hydrogen as well as CO, which should result in performance degradation due to the consumption of hydrogen. Nevertheless, Figure 5.11 shows the great recovery in reverse, which could also be explained by the predominant role of CO over hydrogen in controlling fuel cell performance.

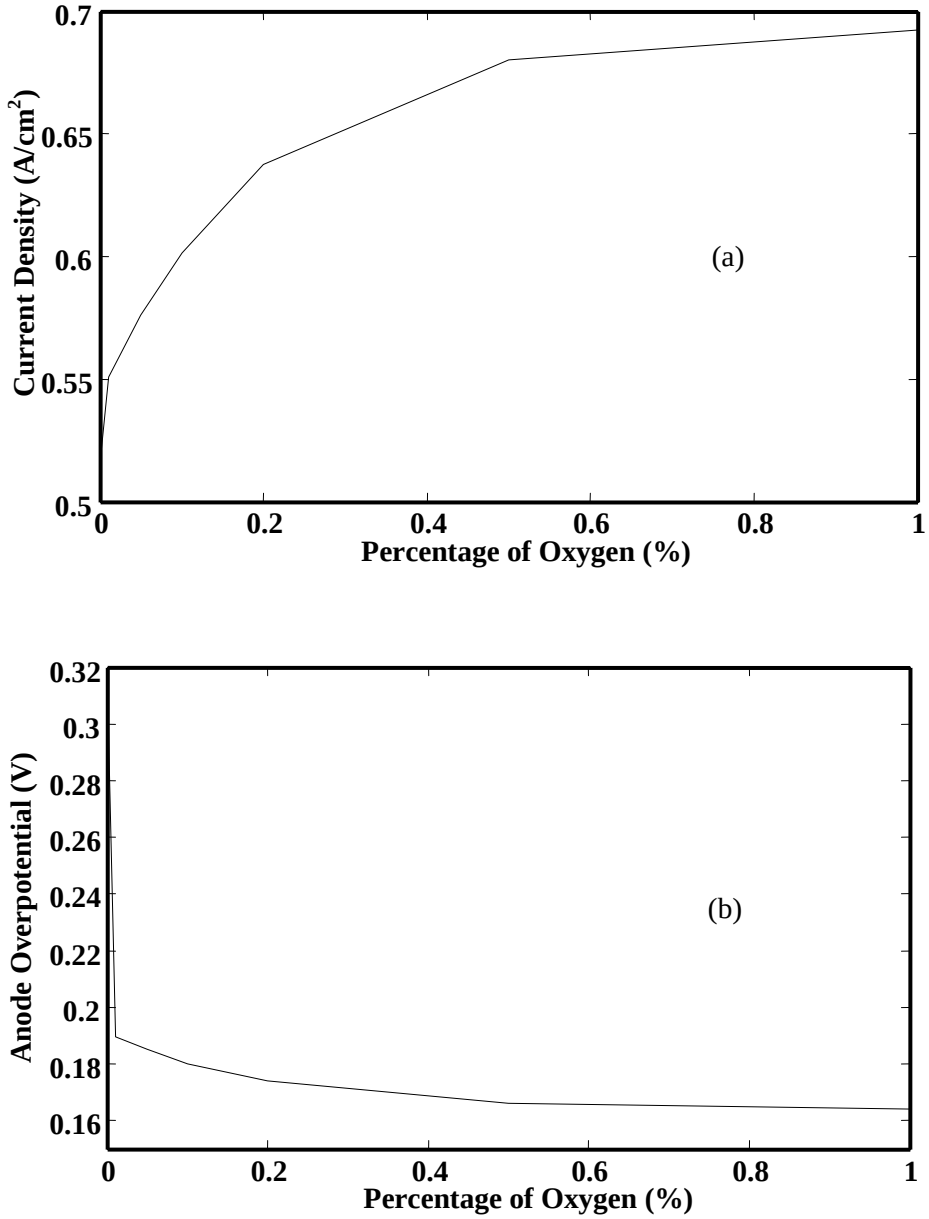

Figure 5.11 (a) Percentage of oxygen vs. current density; (b) Percentage of oxygen vs. anode overpotential.

In addition, 3D figures about oxygen bleeding are examined in Figure 5.12. The coverage distribution of hydrogen is almost the same with Figure 5.6, except that the CO coverage is greater over channel while the oxygen coverage is greater over land area. The reason could be the diffusivity of oxygen is higher than that of CO, so that oxygen could diffuse to the land area more easily. The oxidation rates are found to increase from the inlet to the outlet due to their dependency on the species coverage. Generally, it was always thought that the heterogeneous oxidation was much higher on the CO poisoned sites before; however, it is interesting to find out that the heterogeneous oxidation is highly dependent on oxygen coverage because of its small and sensitive number, which means the heterogeneous oxidation is lower on the CO poisoned sites actually. Physically, since the lower poisoned sites will have a higher reaction rate, so that the recovery on performance by oxygen bleeding will be increased. The results also show that the oxygen bleeding does not remove all adsorbed CO, which is true of the experimental results in [13].

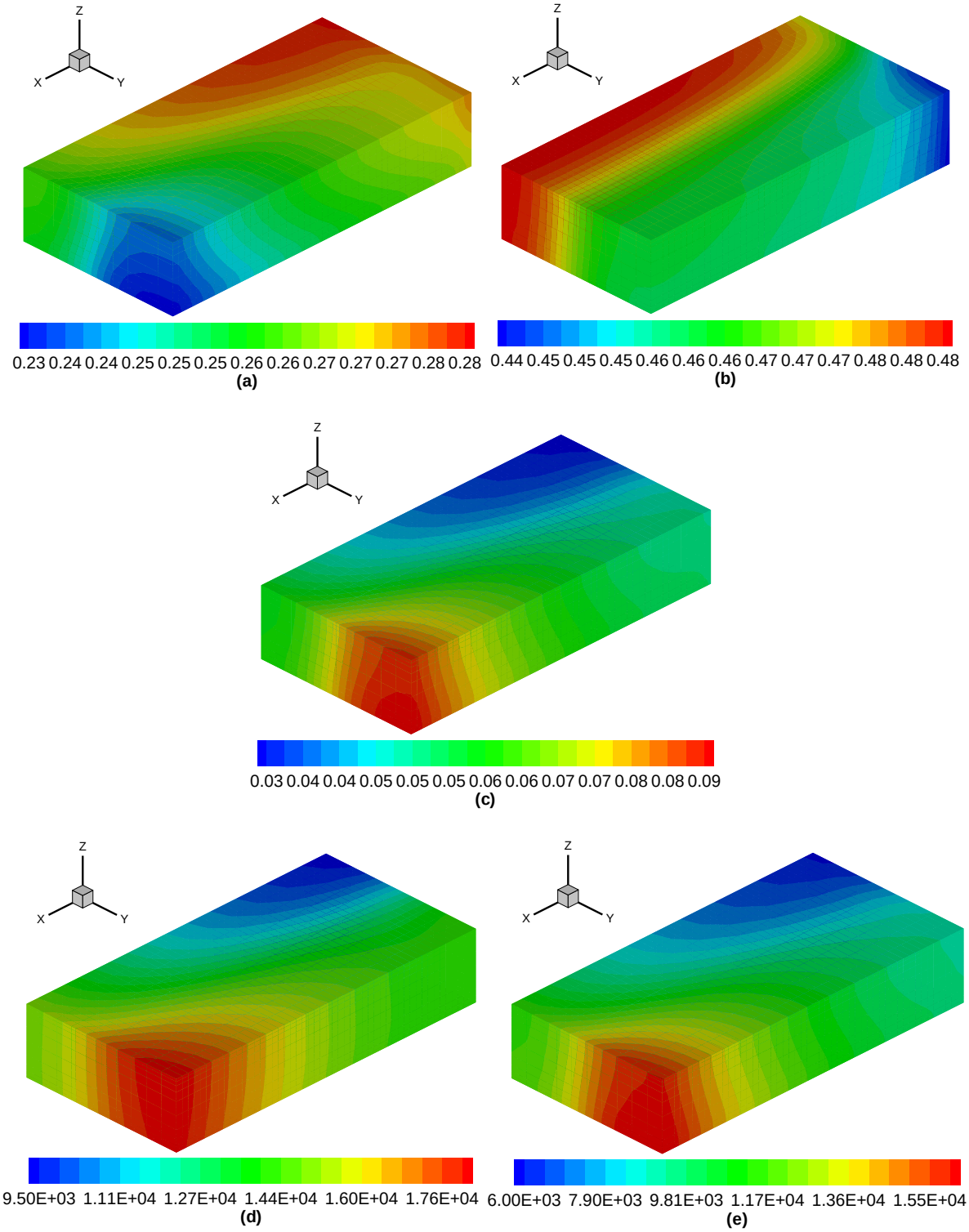

Figure 5.12 (a) Pt-H; (b) Pt-CO; (c) Pt-O; (d) H_2-O_2 oxidation reaction rate (c/m^3.s); (e) CO-O_2 oxidation rate (c/m^3.s).(100 ppm CO+0.5% O_2, the contours are on anode catalyst layer)

5.5 Effect of CO Poisoning and Oxygen Bleeding on Multi-phase Water

Finally, multi-phase water transport phenomena within a single full PEM fuel cell are compared in three cases when the anode fuel is supplied with pure hydrogen, CO poisoned mixture, and CO poisoned mixture with additional oxygen.

Because the fuel used in this study is fully humidified, so the transports of water vapor in these three cases are almost the same. In addition, Figure 5.13 shows CO poisoning effect on dissolved water transport in anode catalyst layer, membrane and cathode catalyst layer. It is interesting to see that the amount of dissolved water in anode catalyst layer is increased due to the CO poisoning. Because of the less oxidation reaction of hydrogen, the dissolved water in cathode catalyst layer is decreased, so is the liquid water shown in Figure 5.14. The additional oxygen in the anode fuel feed can mitigate the performance degradation, thus the dissolved and liquid water in cathode side are produced more by overall electro-chemical reaction. Depending on the distribution of liquid water in cathode, the result shows that the reaction rate adjacent to land area is higher than the reaction rate adjacent to channel and is decreasing along the flow injecting direction. It could be explained by that the liquid water is mainly produced by electro-oxidation of hydrogen, while the small amount produced by electro-oxidation of CO could be ignored.

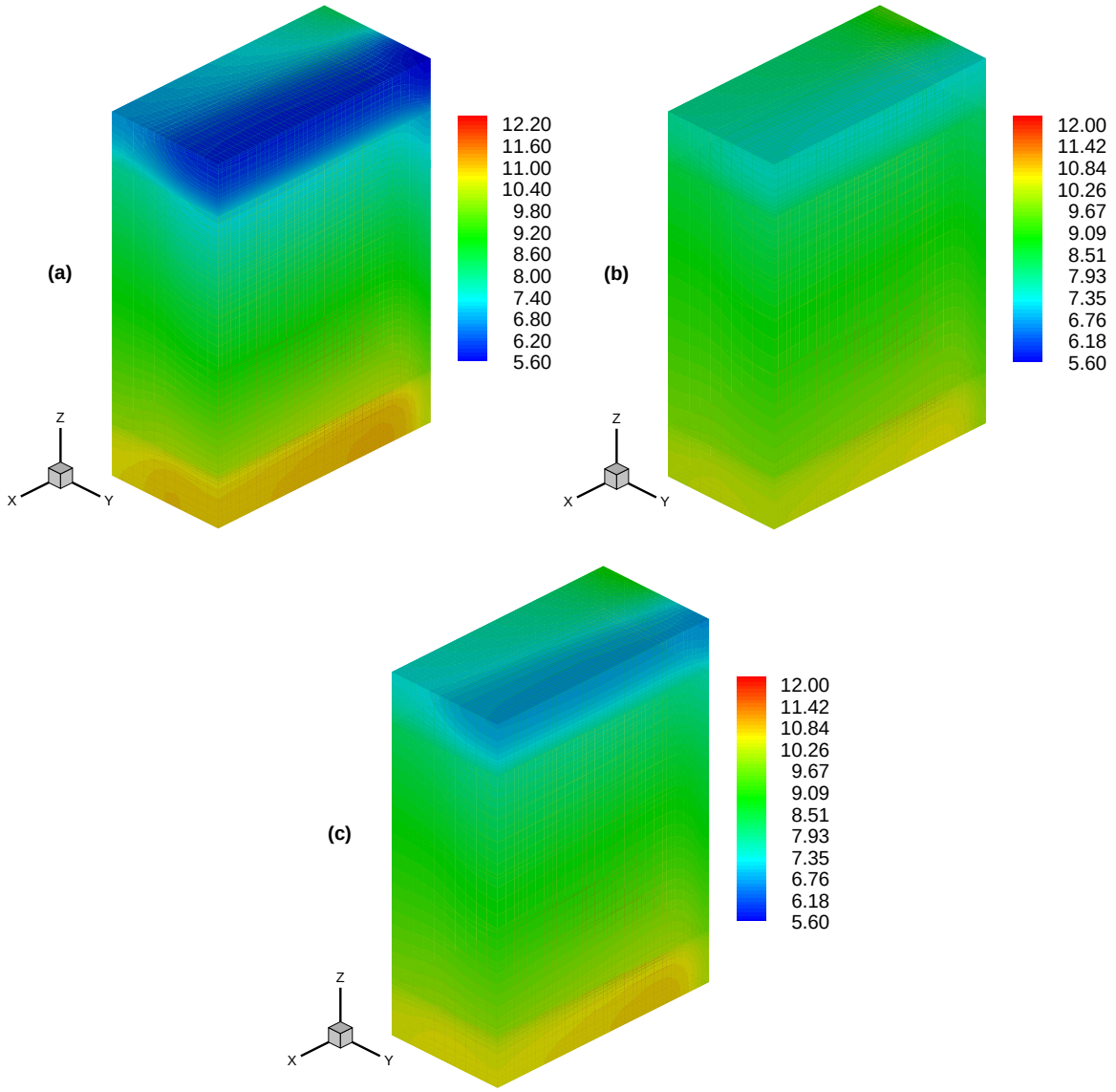

Figure 5.13 Dissolved water in anode catalyst layer (top), membrane (middle), and cathode catalyst layer (bottom) when anode fuel is supplied with (a) pure hydrogen; (b) mixture fuel with 100 ppm CO; (c) mixture fuel with 100 ppm CO and 0.5% oxygen

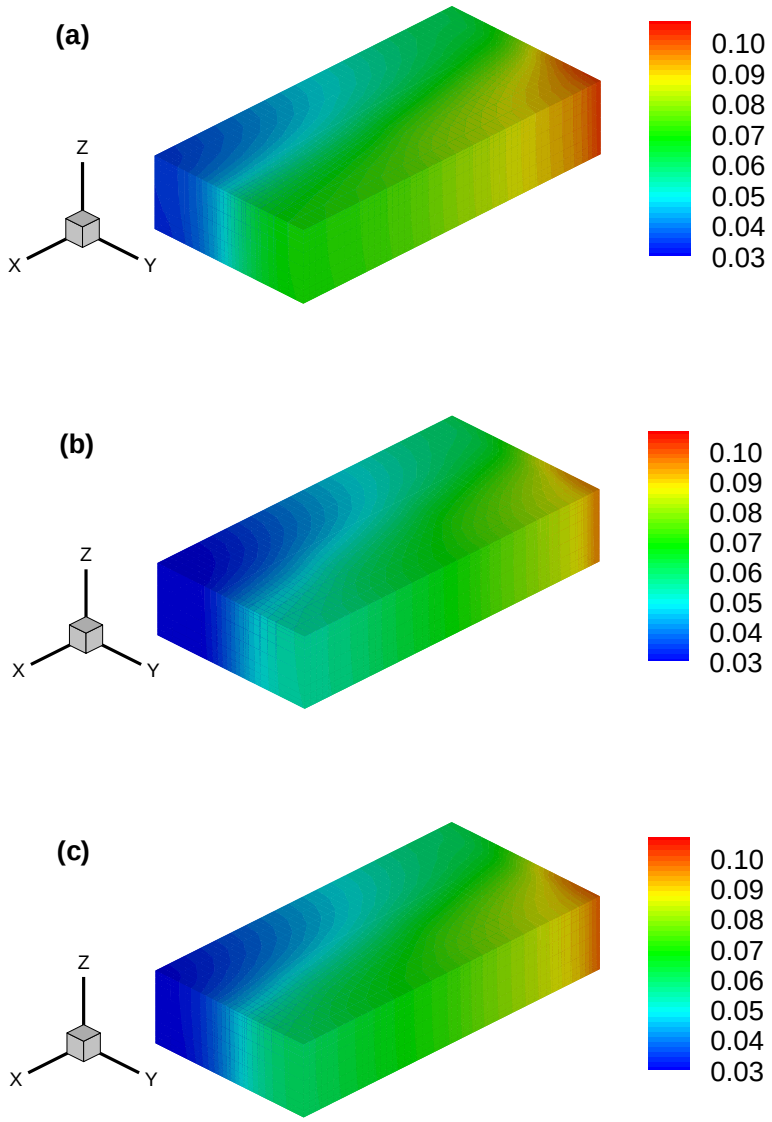

Figure 5.14 Liquid water in cathode catalyst layer when anode fuel is supplied with (a) pure hydrogen; (b) mixture fuel with 100 ppm CO; (c) mixture fuel with 100 ppm CO and 0.5% oxygen

Chapter 6

Results and Discussion – Part II: Transient State

6.1 Validation of Transient Model

After the analysis of CO poisoning and oxygen bleeding effects on fuel cell performance at a steady state, the model is focused on transient state in this part. The model is measured against experimental data, so that the operating conditions for the fuel cell have been changed according to those used in [93]. Both the anode and cathode feed are fully humidified; the inlet gas pressure is 3atm, while the operating temperature is a constant of 80°C; and the stoichiometric ratios are 1.5 and 2.5 at anode and cathode side, respectively. The basic case here is maintained at a specific cell voltage of 0.6 V. The initial condition starts with the absence of CO. The transient model predicts the transient poisoning process very well, as shown in Figure 6.1.

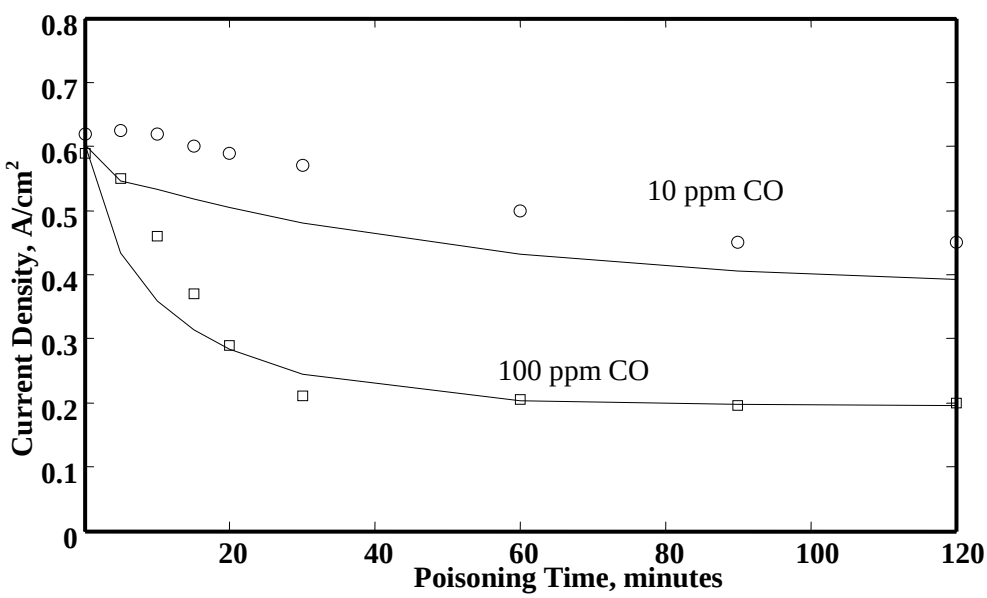

Figure 6.1 Current at 0.6 V during the poisoning process vs. time for two different anode feed gas compositions. The points represent actual experimental results [93], and the curves represent simulations based on the model developed

6.2 Effect of CO Concentration on Fuel Cell Performance

Figure 6.1 also shows that after the pure hydrogen is switched to a gas mixture containing 10 ppm or 100 ppm CO, the current density decreases dramatically. It drops from 0.6 A/cm^2 to 0.45 A/cm^2 for 10 ppm CO and to 0.2 A/cm^2 for 100 ppm CO, respectively. The aim of this simulation is to determine the characteristic time of poisoning and recovery starting from a pseudo-steady state. It is found that the performance of the fuel cell declines extremely fast during the first 10 min since the feed stream has been contaminated, however the change is mitigated as the time is increasing and the current density becomes stabilized after 2 h for 10 ppm CO case, and 40 min for 100 ppm CO case. The numerical result is the right fit for the assumption that additional CO can slow the hydrogen adsorption and the slow degree is dependent of CO quantity [66]. Thus, a large amount of CO will degrade the performance of the fuel cell significantly in a short period. In addition, Figure 6.2 shows that the coverage of hydrogen descends from 0.78 to 0.25 for 10 ppm case and 0.06 for 100 ppm case; while Figure 6.3 shows that the CO coverage increases from 0 to 0.6 and 0.82, respectively. It results from high sticking probability of CO on platinum. However, the higher sticking probability does not mean the higher adsorption rate of CO on platinum than that of hydrogen; it depends on the difference of adsorption, desorption, and electro-oxidation rates.

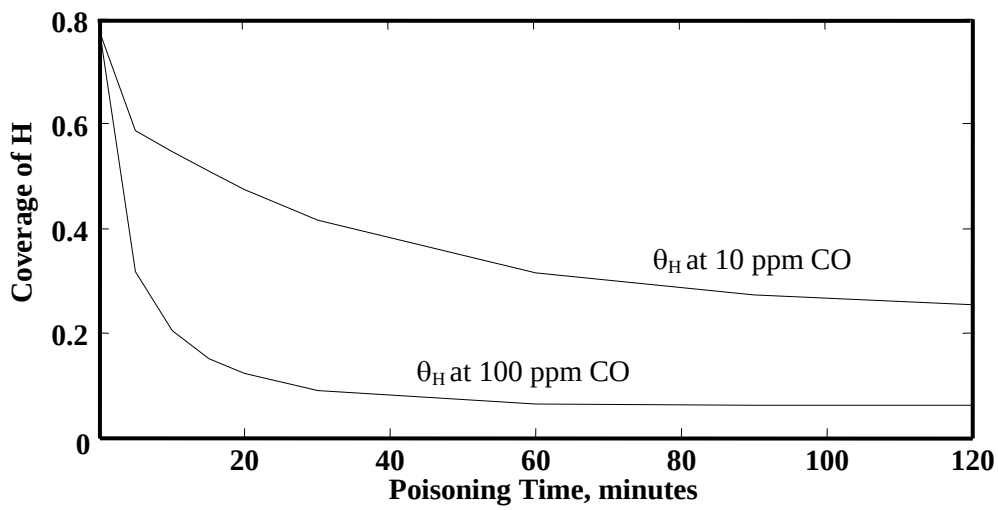

Figure 6.2 The coverage of hydrogen on anode catalyst layer

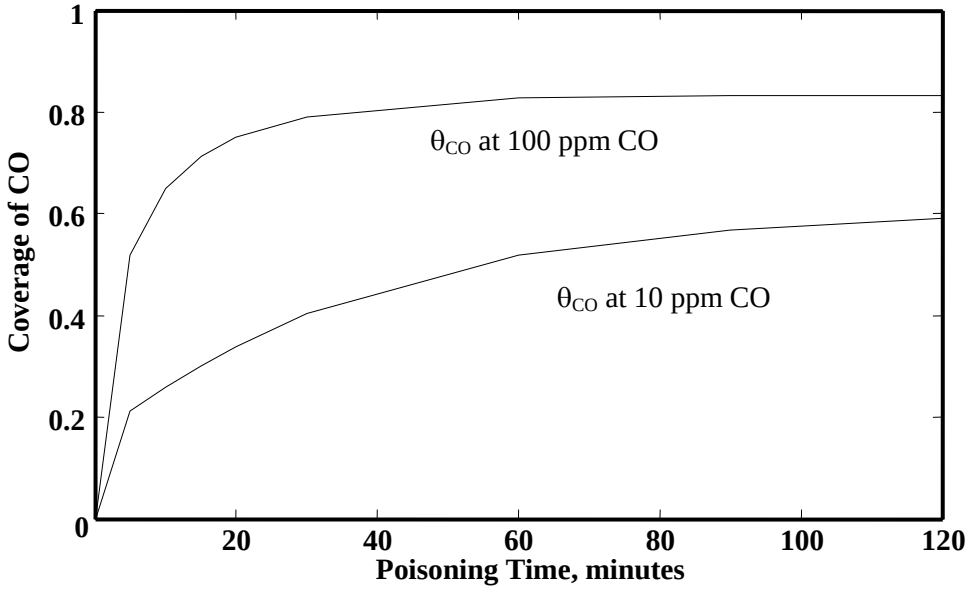

Figure 6.3 The coverage of CO on anode catalyst layer

In Figure 6.4 and Figure 6.5, after 100 ppm CO is added into anode fuel stream, it is obviously seen that the adsorption rate of hydrogen on anode catalyst layer is almost 4-orders of the CO adsorption rate. However, the desorption rate and electro-oxidation rate of hydrogen are also very high at the beginning; while those rates of CO are almost zero. Hence, most of the adsorbed hydrogen is consumed; while most of the adsorbed CO is still sticking to the platinum surface. Moreover, Figure 6.5 shows an interesting phenomenon that the desorption rate of CO has a minor increment at the beginning, and then it is decreasing gradually.

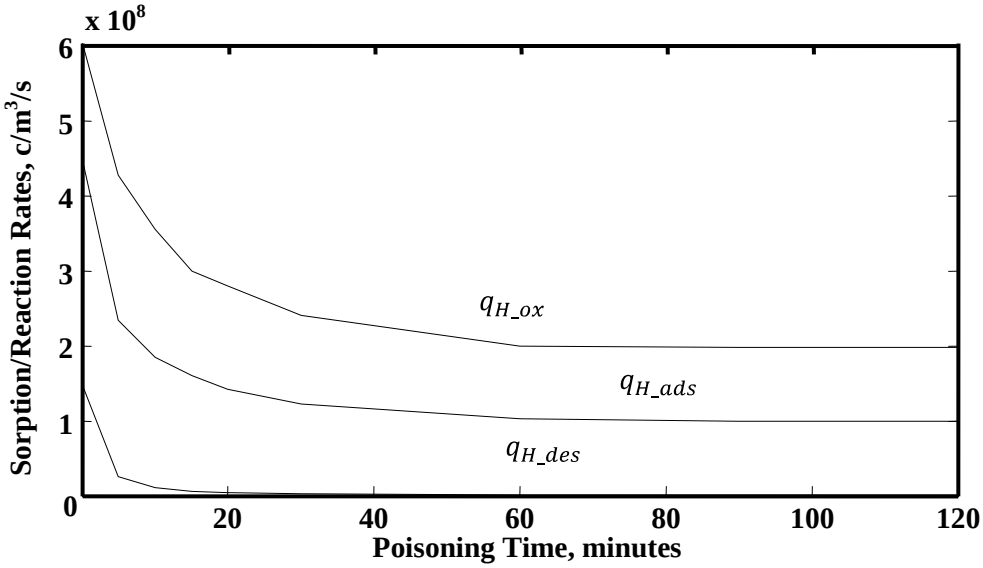

Figure 6.4 The adsorption/desorption rates and electro-oxidation rate of hydrogen on anode catalyst layer

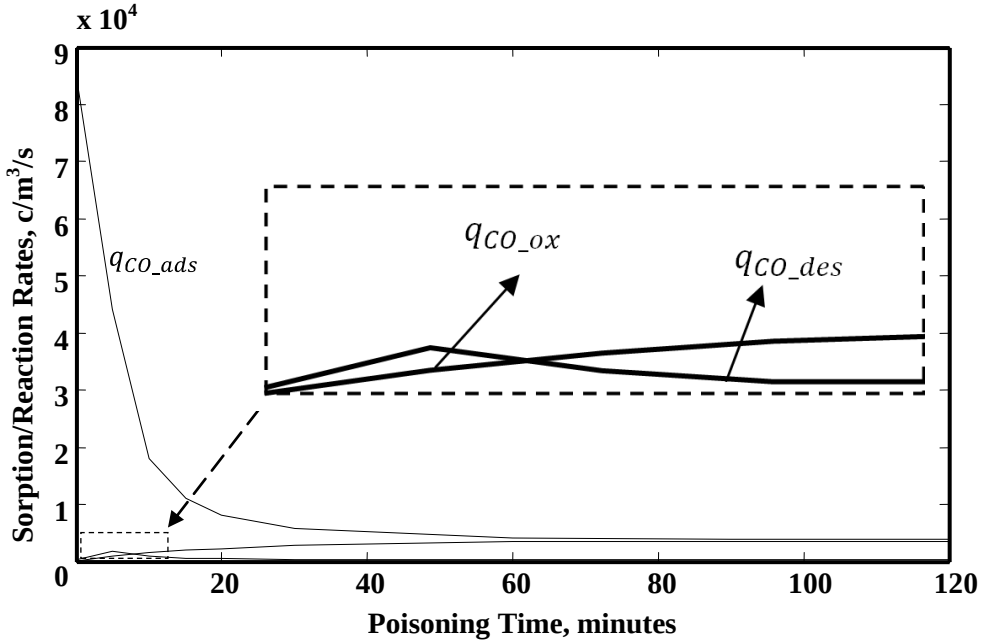

Figure 6.5 The adsorption/desorption rates and electro-oxidation rate of CO on anode catalyst layer

The electro-oxidation rate of adsorbed hydrogen is shown in 3D contours in Figure 6.6. As the poisoning is processing, the electro-oxidation of hydrogen is decreasing dramatically, resulting in a poor cell performance. After 50 minutes, the PEM fuel cell has almost been blocked by CO, little current density is produced by the electro-chemical reaction. Moreover, it is interesting to find that both the plate land area and the bottom of the anode catalyst layer have higher hydrogen reaction rates, resulting in a higher current density. Because CO diffusion is less than hydrogen's, therefore these sites have less CO poisoning effect.

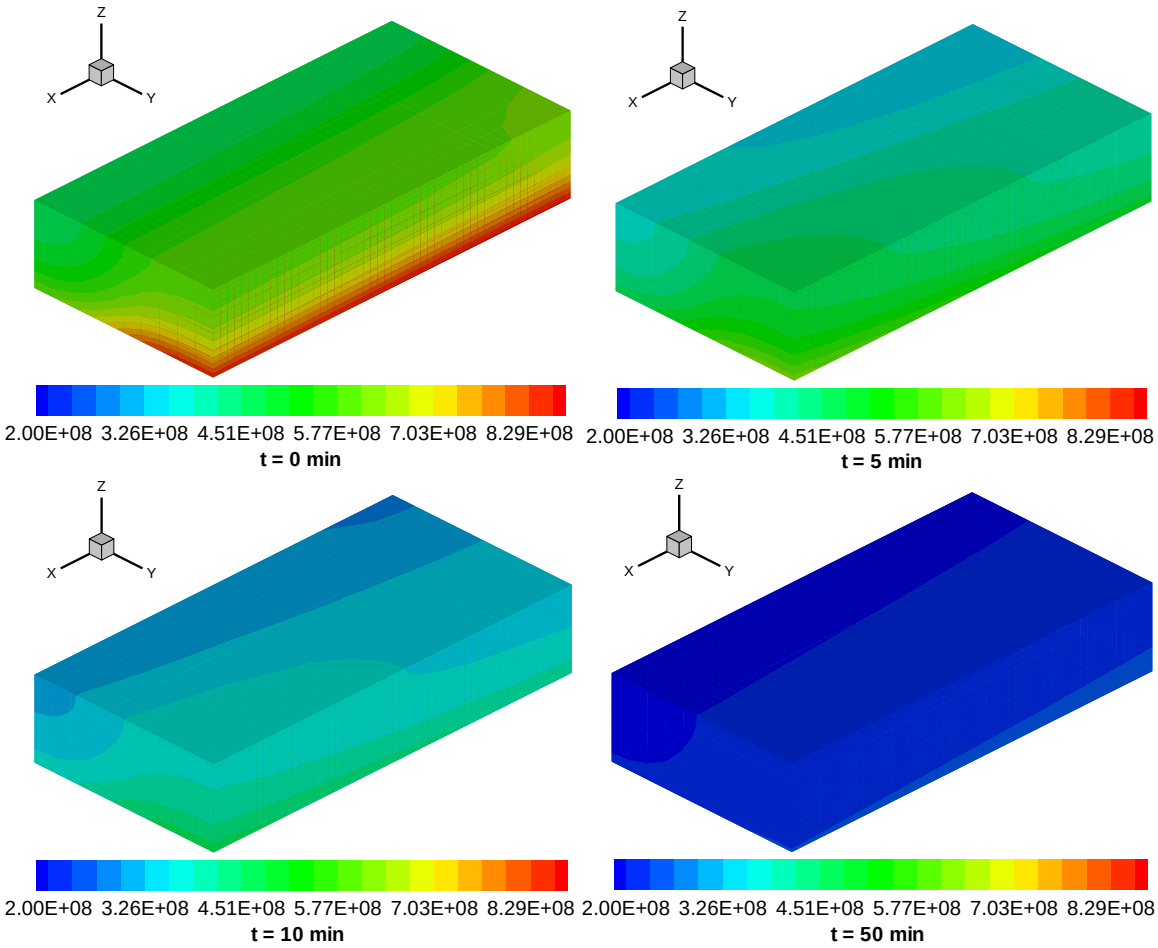

Figure 6.6 The electro-oxidation rate of hydrogen in anode catalyst layer ($c/m^3.s$)

6.3 Effect of Cell Voltage on Fuel Cell Performance

When the fuel cell stack undergoes a perturbation, such as the sudden change of load, like speeding up, slowing down, or a shut-down, it is the transient model that will be able to simulate these real situations.

In Figure 6.7, the transient process is divided into 4 periods. The initial state of fuel cell runs at 0.6 V. Then the cell voltage is increased to 0.7 V at 50 minutes and to 0.5 V at 220 minutes, finally is returned to 0.6 V at 400 minutes. The current density changes according to the shifts of cell voltage. Another interesting phenomenon is found that there are short fluctuations after each cell voltage switch. They are named as overshoot and undershoot in other works [71, 72], which are believed to be caused by transient species transport. Take the second period as an example, since there is low oxygen concentration leftover when the cell voltage starts to change from 0.6 V to 0.7 V; so there is an undershoot at the beginning, then the oxygen concentration recovers gradually as the consumption of oxygen is decreasing to a certain level. Moreover, it is obviously seen that the undershoot is smaller at lower current density, which means fuel cell performance is more stabilized at low current density, because of the slight degree of CO poisoning.

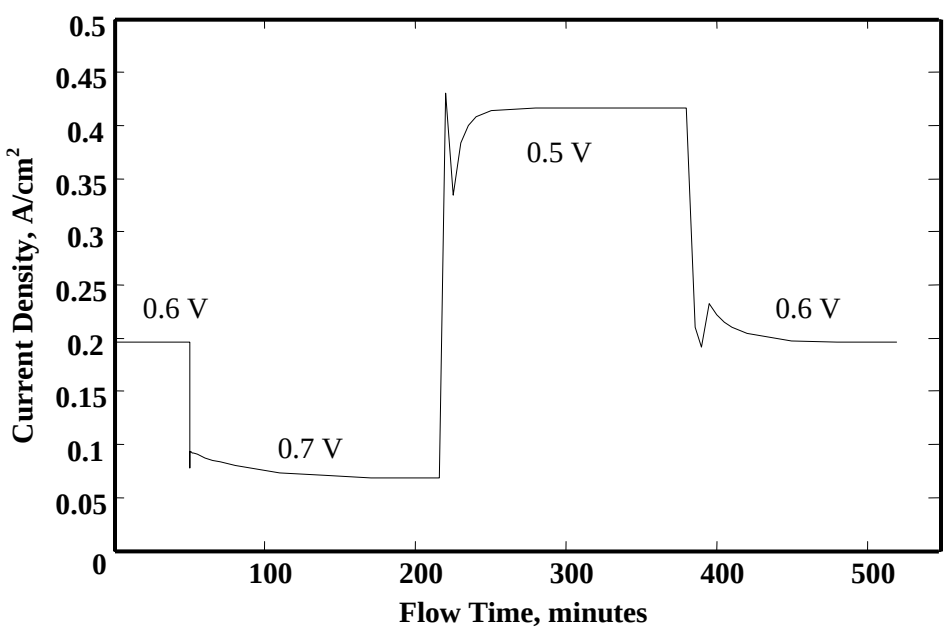

Figure 6.7 Current density changes according to cell voltage

In addition, at the contamination level with 100 ppm CO, increasing cell voltage means decreasing current density, hence, the overpotential decreases as well, because less activation potential is needed for low current density as shown in Figure 6.8. Also, there is only a slight undershoot of anode overpotential at low current density.

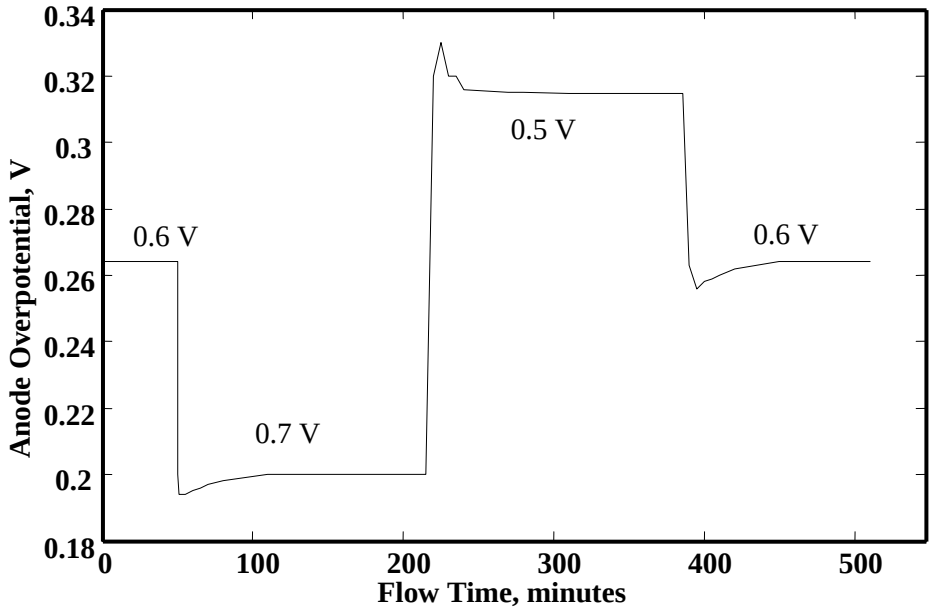

Figure 6.8 Anode overpotential changes according to cell voltage

In the second period, Figure 6.9 shows that the coverage of CO on platinum surface is increasing gradually, since the production of low current density does not need much catalyst area for hydrogen adsorption. Vice versa, during the third period, the coverage of CO is decreasing quickly due to the high current density demand. Worth to point out, as the conclusion made in the steady state part, CO poisoning effect is highlighted at high current density. Consequently, the time cost to arrive steady state during the third period is much quicker than the second period; even its CO coverage is lower.

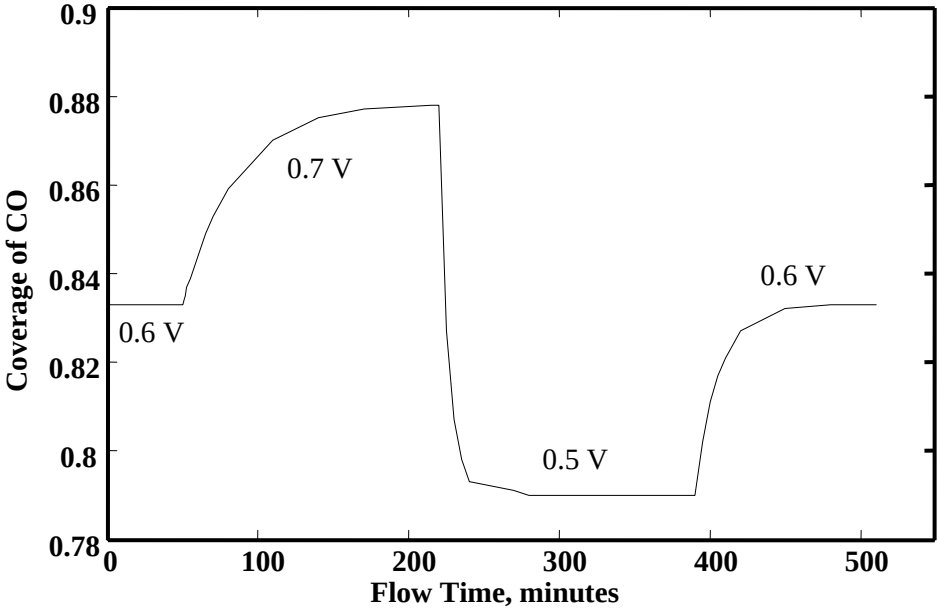

Figure 6.9 Coverage of CO changes according to cell voltage

However, the change of hydrogen coverage in anode catalyst layer in Figure 6.10 is different with that of CO in Figure 6.9. It is clear to see that the coverage of CO is changing gradually, while the hydrogen coverage has a sudden raise, then drops to a certain level in the second and fourth periods. It can be explained by the demand of adsorbed hydrogen on the anode catalyst layer for electro-oxidation is suddenly dropped due to the lower current density. Thus, the leftover hydrogen increases abruptly. Nevertheless, the coverage of CO expands its space gradually leading to the coverage of hydrogen has to be shrunken eventually. Vice versa, during the third period, the coverage of hydrogen has a sudden decline, and then climbs up finally.

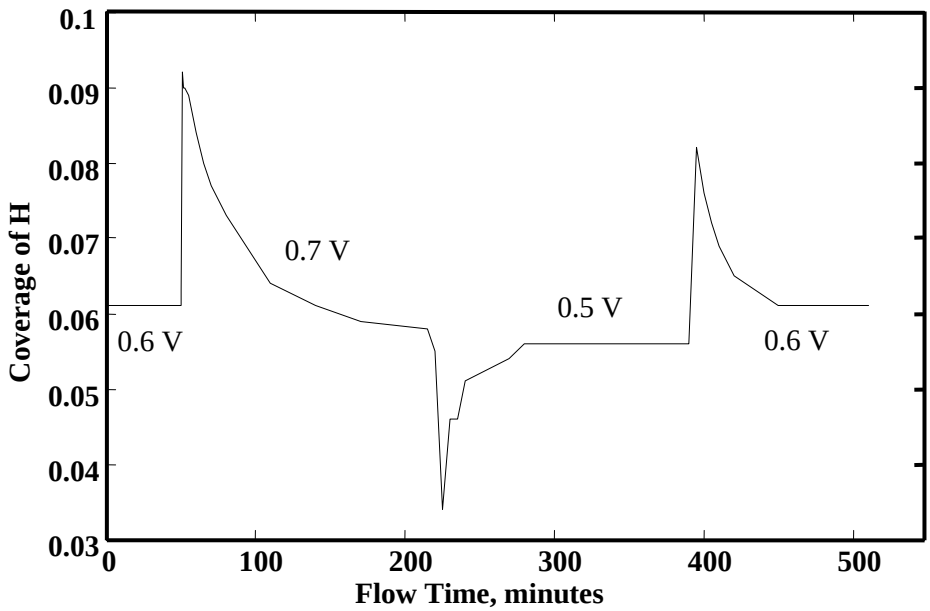

Figure 6.10 Coverage of hydrogen changes according to cell voltage

6.4 Recovery of Fuel Cell Performance

The reversible issue of the CO poisoning process is investigated as well. The result shows that the fuel cell performance is completely reversible after the anode fuel stream has been switched from contaminated mixture back to pure hydrogen supply. In Figure 6.11, the fuel cell starts from initial condition with pure hydrogen; then, the anode fuel feed is added with 100 ppm CO impurity. The current density drops markedly from 0.6 A/cm^2 to 0.2 A/cm^2, and the slope is extremely steep at the beginning. After 120 minutes, the anode fuel feed is changed to pure hydrogen again. The result shows a good phenomenon that the current density could return to 0.6 A/cm^2 eventually, which is also approved in [63]. However, the recovery process takes much more time. Since the high sticking probability of CO on platinum makes the catalyst layer be hard to get rid of adsorbed CO. Thus, the recovery process is as 3 times long as it is for degradation in this case.

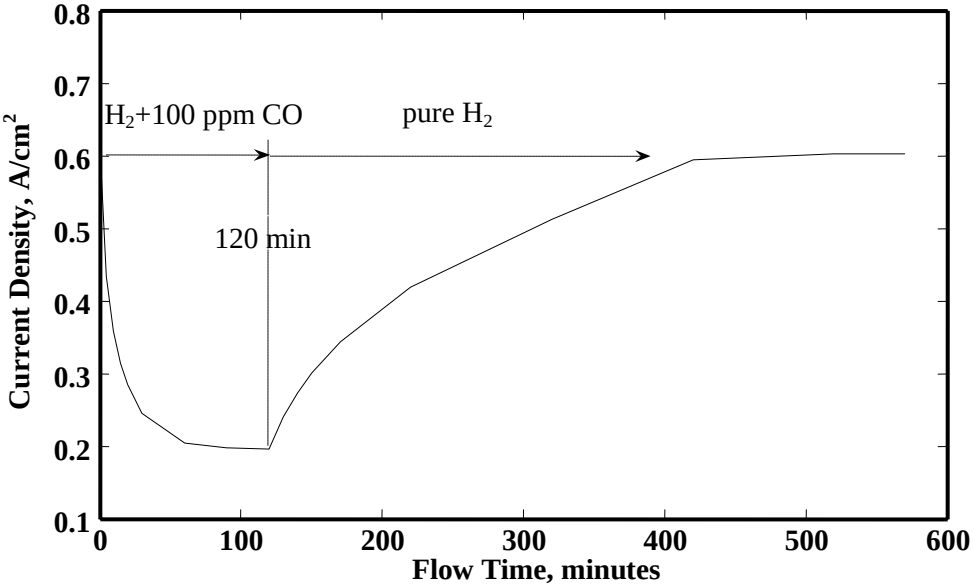

Figure 6.11 The change of current density according to anode fuel feed switches

In addition, the 3D contours about electro-oxidation rate of hydrogen in the anode catalyst layer in Figure 6.12 explain the change of current density well. Since, the electro-oxidation rate of CO is extremely small, which could be ignored in electricity production. The 3D figures show that there is a minimum point at 120 minutes and a whole recovery at 500 minutes.

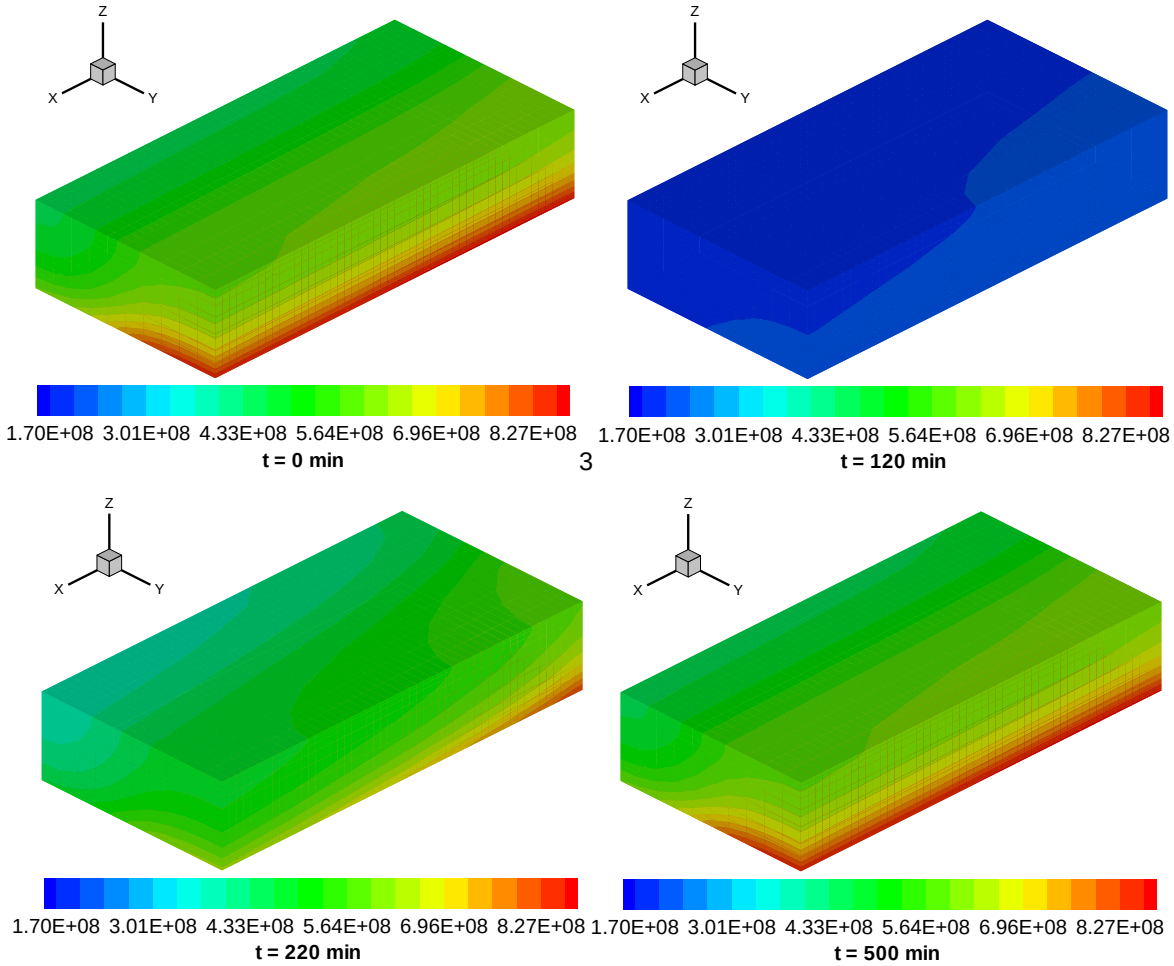

Figure 6.12 The 3D distribution of hydrogen electro-oxidation rate (c/m^3.s) in anode catalyst layer according to time steps used in Figure 6.11

The result shows almost full recovery of fuel cell performance after inputting pure hydrogen instead of contaminated anode supply. Also, adding oxygen into the contaminated anode fuel can mitigate CO poisoning effect. Figure 6.13 shows that there is a lag phenomenon of recovery at the beginning, since oxygen bleeding needs some time to be active due to the well-established Pt-CO bond. But the fuel cell performance does recover quickly and greatly after a short period. Hence, oxygen bleeding is still a good choice for fuel cell application with CO poisoning issue.

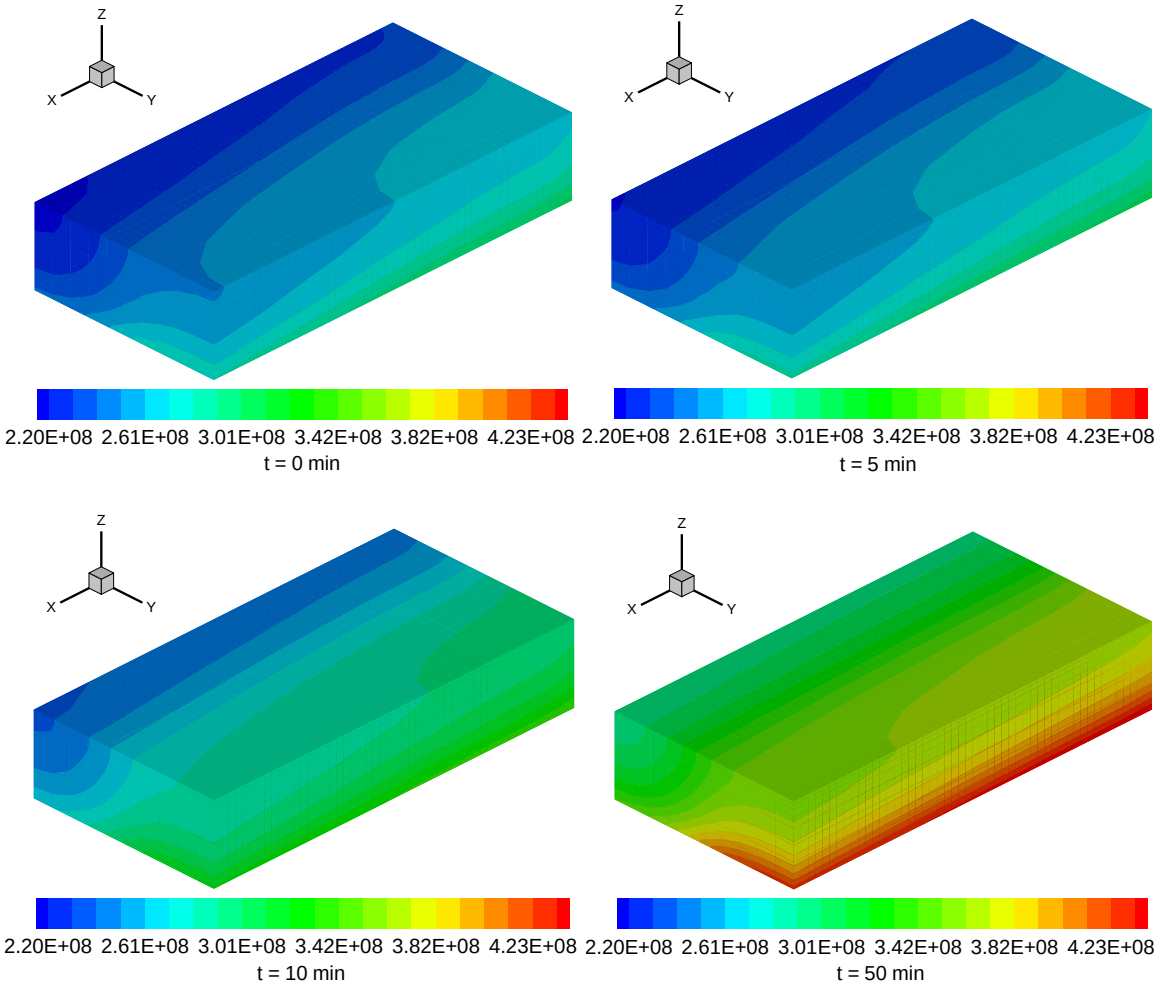

Figure 6.13 The recovery of hydrogen electro-oxidation rate (c/m^3.s) in anode catalyst layer when 0.5% O_2 is added into anode mixture fuel with 100 ppm CO

Chapter 7
Conclusions and Recommendations

A 3D multi-phase model of PEM fuel cell with CO poisoning and oxygen bleeding has been developed in this thesis research, based on the reactant-pair mechanism for CO poisoning, Tafel-Volmer mechanism for hydrogen electrooxidation and oxygen reduction reactions, and Langmuir-Hinshelwood mechanism for oxygen bleeding. The model has been validated by comparing with experimental results. It has been found that the key drive for the fuel cell performance change is affected by the adsorption rates, desorption rates, and electro-oxidation rates of hydrogen and CO, which result in high sticking probability of CO on platinum surface compared with that of hydrogen, explaining the degradation of fuel cell performance. Thus, by increasing the concentration of CO results in a drastic decrease in cell performance due to the increment of CO coverage on the platinum surface. Moreover, a large amount of CO results in a much faster degradation process. Then, 3D distributions of various parameters are illustrated to explain the CO poisoning effect inside the anode catalyst layer. At the flow exit, the portion of anode catalyst layer close to GDL under flow channel is found to have the most significant poisoning effect. The result helps optimize the distribution of platinum on anode catalyst layer during the manufacturing. The distribution of hydrogen coverage with pure hydrogen feed is different from that after the feed is contaminated by the CO. The adsorption rate of CO is decreasing along the channel with low impurity fuel while it is increasing along the channel at high impurity mixture. Furthermore, the performance of the fuel cell poisoned by CO could be recovered after reinvesting pure hydrogen. The reaction rate is first recovered at the flow inlet and then along the flow direction. The addition of oxygen into the anode fuel stream can help in alleviating the CO poisoning effect, the recovery rate is found to be higher near outlet than inlet at the beginning, and then it becomes more evenly distributions along the channel. Lastly, the analysis of change of cell voltage simulating the sudden load change in reality helps predict that the poisoned PEM fuel cell system is more stable at a low load driving situation. Generally, the results obtained from this 3D model can help researchers understand CO poisoning phenomena and oxygen bleeding to reduce the cost for cell design, improve the durability when driving at a low load, and increase the performance when applying oxygen bleeding. Yet, there are still many other impurities in fuel stream, like H_2S and CO_2. In addition, research on the effect of fuel crossover still needs more work, since CO may cross the membrane to the cathode side through pin holes; and oxygen may travel from the cathode to the anode due to the concentration and pressure gradients.

Bibliography

1. X. Li, *Principles of Fuel Cells*, Taylor & Francis, 2005.

2. S. Srinivasan, R. Mosadle, P. Stevens, and C. Yang, Fuel Cells: Reaching the Era of Clean and Efficient Power Generation in the Twenty-First Century. *Annual Review of Energy and the Environment*, 24:281-328, 1999.

3. N. Zamel, X. Li, Effect of contaminants on polymer electrolyte membrane fuel cells, *Progress in Energy and Combustion Science*, doi:10.1016/j.pecs.2010.06.003.

4. K. Jiao, X. Li, Water transport in polymer electrolyte membrane fuel cells, *Progress in Energy and Combustion Science*, doi:10.1016/j.pecs.2010.06.002.

5. A. Levitz, Two-Dimensional Modeling of a Liquid-Feed Direct Methanol Fuel Cell, *Master thesis*, University of Waterloo, 2003.

6. D.P. Wilkinson, D. Thompsett, O. Savadogo, P.R. Roberge, *Proceedings of the Second National Symposium on New Materials for Fuel Cell and Modern Battery Systems*, Montreal, Quebec, 1997.

7. H. Wu, Mathematical Modeling of Transient Transport Phenomena in PEM Fuel Cells, *PhD thesis*, University of Waterloo, 2009.

8. G. Hoogers, *Fuel Cells Technology Handbook*, CRC Press, 2002.

9. N. Sammes, *Fuel Cells Technology: Reaching Towards Commercialization*, Springer, 2006.

10. Z. Shi, D. Song, J. Zhang, Z. Liu, S. Knights, R. Vohra, N. Jia, and D. Harvey, Transient Analysis of Hydrogen Sulfide Contamination on the Performance of a PEM Fuel Cell, *Journal Electrochemical Society*, 154:B609-B615, 2007.

11. Z. Qi, C. He, and A. Kaufman, Effect of CO in the anode fuel on the performance, *Journal of Power Sources*, 111:239-247, 2002.

12. P. Stonehart and P. Ross, The commonality of surface processes in electrocatalysis and gas-phase heterogeneous catalysis, *Catalysis Reviews Science and Engineering*, 12:1-35, 1975.

13. T. Tingelofa, L. Hedstromb, N. Holmstroma, P. Alvforsb, and G. Lindbergha, The influence of CO_2, CO and air bleed on the current distribution of a polymer electrolyte fuel cell, *International Journal of Hydrogen Energy*, 33:2064 -2072, 2008.

14. T. Smolinka, M. Heinen, Y. Chen, Z. Jusys, W. Lehnert, and R. Behm, CO_2 reduction on Pt electrocatalysts and its impact on H_2 oxidation in CO_2 containing fuel cell feed gas – A combined in situ infrared spectroscopy, mass spectrometry and fuel cell performance study, *Electrochimica Acta*, 50:5189-5199, 2005.

15. Q. Li, R. He, J. Gao, J. Jensen, and N. Bjerrum, The CO poisoning effect in PEMFCs operational at temperatures up to 200°C, *Journal of The Electrochemical Society*, 150:A1599-A1605, 2003.

16. R.J. Bellows, E.P. Marucchi-Soos, and D.T. Buckley, Analysis of Reaction Kinetics for Carbon Monoxide and Carbon Dioxide on Polycrystalline Platinum Relative to Fuel Cell Operation, *Industrial & Engineering Chemistry Research*. 35:1235-1242, 1996.

17. D.T. Chin, and P.D. Howard, Hydrogen Sulfide Poisoning of Platinum Anode in Phosphoric Acid Fuel Cell Electrolyte, *Journal of The Electrochemical Society*,2447-2451, 1986.

18. T.H. Gardner, D.A. Berry, K.D. Lyons, S.K. Beer, and A.D. Freed, Fuel processor integrated H_2S catalytic partial oxidation technology for sulfur removal in fuel cell power plants, *Fuel*, 81:2157-2166, 2002.

19. R. Mohtadi, W.K. Lee, S. Cowan, and J. Zee, Effects of Hydrogen Sulfide on the Performance of a PEMFC, *The Journal of Electrochemical Society*, 6:A272-A274, 2003.

20. R. Mohtadi, W.K. Lee, J. Zee, The effect of temperature on the adsorption rate of hydrogen sulfide on Pt anodes in a PEMFC, *Applied Catalysis B: Environmental*, 56:37-42, 2005.

21. F. Uribe and T. Zawodziniski, Jr., *200th Meeting of The Electrochemistry Society*, San Francisco, CA, Abstracts 339, Sept. 2001.

22. G. Janssen, Modelling study of CO_2 poisoning on PEMFC anodes, *Journal of Power Sources*, 136:45-54, 2004.

23. F. Bruijn, D. Papageorgopoulos, E. Sitters and G. Janssen, The influence of carbon dioxide on PEM fuel cell anodes, *Journal of Power Sources*, 110:114-124, 2002.

24. T. Ralph and M. Hogarth, Catalysis for low temperature fuel cells, *Platinum Met Rev.* 46:117-135, 2002.

25. A. Becdelievre, J. Becdelievre, and J. Clavilier, Electrochemical oxidation of adsorbed carbon monoxide on platinum spherical single crystals, Effect of anion adsorption, *Journal of Electroanalytical Chemistry and Interfacial Electrochemistry*, 294:97-110, 1990.

26. M. Ciureanu and H. Wang, Electrochemical impedance study of anode CO-poisoning in PEM fuel cells, *Journal of New Materials for Electrochemical Sys*tems, 3:107-119, 2000.

27. J. Kim, Y. Park, K. Kobayashi, M. Nagai, Effect of CO Gas and Anode−Metal Loading on H_2 Oxidation in Proton Exchange Membrane Fuel Cell, *Journal of Power Sources*, 103-127, 2001.

28. J. Kim, Y. Park, K. Kobayashi, M. Nagai, Characterization of CO tolerance of PEMFC by ac impedance spectroscopy, *Solid State Ionics*, 140:313–325, 2001.

29. M. Wilson, C. Derouin, J. Valerio, T. Zawodzinski, S. Gottesfeld, Electrocatalysis Issues in Polymer Electrolyte Fuel Cells, *Proceedings of the 28th IECEC Conference*, Atlanta, 1993.

30. A. Rodrigues, J. Amphlett, R. Mann, B. Peppley and P. Roberge, Carbon monoxide poisoning of proton exchange membrane fuel cells, IECEC-97, *Proceedings of the 32nd Intersociety Energy Conversion Engineering Conference*, Honolulu, HI, USA, 1997.

31. R. Lemons, Fuel Cells for Transportation, *Journal of Power Sources*, 29:251-264, 1990.

32. V. Schmidt, P. Brockerhoff, B. Hohlein, R. Menzer, U. Stimming, Utilization of methanol for polymer electrolyte fuel cells in mobile systems, *Journal of Power Sources*, 49:299-313, 1994.

33. R. Benesch, T. Jacksier, *2005 IEEE Vehicle Power and Propulsion Conference*, 2006.

34. R. Jiang, H.R. Kunz and J.M. Fenton, Influence of temperature and relative humidity on performance and CO tolerance of PEM fuel cells with Nafion®–Teflon®–$Zr(HPO_4)^2$ higher temperature composite membranes, *Electrochimica Acta*, 51:5596-5605, 2006.

35. J. Divisek, H.F. Oetjen, V. Peinecke, V.M. Schmidt and U. Stimming, Components for PEM fuel cell systems using hydrogen and CO containing fuels, *Electrochimica Acta*, 43:3811-3815, 1998.

36. J.J. Baschuk and X. Li, Carbon monoxide poisoning of proton exchange membrane fuel cells, *International Journal of Energy Research*, 25:695-715, 2001.

37. H.F. Oetjen, V.M. Schmidt, U. Stimming, F. Trila, Performance Data of a Proton Exchange Membrane Fuel Cell Using H_2/CO as Fuel Gas, *Journal of The Electrochemical Society*, 143:3838-3842, 1996.

38. L. Gubler, G.G. Scherer and A. Wokaun, Effects of cell and electrode design on the CO tolerance of polymer electrolyte fuel cells, *Physical Chemistry Chemical Physics*, 3:325-329, 2001.

39. A. Taniguchi, T. Akita, K. Yasuda, and Y. Miyazaki, Analysis of electrocatalyst degradation in PEMFC caused by cell reversal during fuel starvation, *Journal of Power Sources*, 130:42-49, 2004.

40. T. Zhou and H. Liu, A 3D model for PEM fuel cells operated on reformate, *Journal of Power Source*, 138:101-110, 2004.

41. J. Zhang, T. Thampan, and R. Datta, Influence of anode flow rate and cathode oxygen pressure on CO poisoning of proton exchange membrane fuel cells, *Journal of The Electrochemical Society*, 149:A765-A772, 2002.

42. T. Gu, W.K. Lee, J. Zee, and M. Murthy, Effect of Reformate Components on PEMFC Performance, *Journal of Electrochemical Society*, 151:A2100-A2105, 2004.

43. X. Cheng, Z. Shi, N. Glass, L. Zhang, J. Zhang, D. Song, Z. Liu, H. Wang and J. Shen, A review of PEM hydrogen fuel cell contamination: Impacts, mechanisms, and mitigation, *Journal of Power Sources*, 165:739-756, 2007.

44. M. Koper, T. Shubina, and R. Santen, Periodic Density Functional Study of CO and OH Adsorption on Pt-Ru Alloy Surfaces: Implications for CO Tolerant Fuel Cell Catalysts, *Journal phys. Chem.*, 106(3):686-692, 2002.

45. B. Steele and A. Heinzel, Materials for fuel-cell technologies, *Nature International Weekly Journal of Science*, 414:345-352, 2001.

46. J.H. Wee, K.Y. Lee, Overview of the development of CO-tolerant anode electrocatalysts for proton-exchange membrane fuel cells, *Journal of Power Sources*, 157:128-135, 2006.

47. R.C. Urian, A.F. Gulla, and S. Mukerjee, Electrocatalysis of reformate tolerance in proton exchange membranes fuel cells: Part I, *Journal of Electroanalytical Chemistry*, 554-555:307-324, 2003.

48. H. Yu, Z. Hou, B. Yi, Z. Lin, Composite anode for CO tolerance proton exchange membrane fuel cells, *Journal of Power Sources*, 105:52-57,2002.

49. C.H. Wan, Q.H. Zhuang, Novel layer wise anode structure with improved CO-tolerance capability for PEM fuel cell, *Electrochimica Acta*, 52:4111-4123, 2007.

50. W. Shi, M. Hou, Z. Shao, J. Hu, Z. Hou, P. Ming, B. Yi, A novel proton exchange membrane fuel cell anode for enhancing CO tolerance, *Journal of Power Sources*, 174:164-169, 2007.

51. S. Kawatsu, Fuel-cells generator system and method of generating electricity from fuel cells, *Patent No. 5,925,476*, Jul.20, 1999.

52. M. Murthy, M. Esayian, W.K. Lee, J. Zee, The Effect of Temperature and Pressure on the Performance of a PEMFC Exposed to Transient CO Concentrations, *Journal of the Electrochemical Society*, 150:A29-A34, 2003.

53. B. Lakshmanan, W. Huang, and J.W. Weidnera, Electrochemical Filtering of CO from Fuel-Cell Reformate, *The Electrochem. Solid-State Lett.*, 5: A267-A270, 2002.

54. T.E. Springer, T. Rockward, T.A. Zawadzinski and S. Gottesfeld, Model for Polymer Electrolyte Fuel Cell Operation on Reformate Feed, Effects of CO, H_2 Dilution, and High Fuel Utilization, *Journal Electrochemical Society*, 148:A11-A23, 2001.

55. L.P.L. Carrette, K.A. Friedrich, M. Huber and U. Stimming, Improvement of CO tolerance of proton exchange membrane (PEM) fuel cells by a pulsing technique, *Journal Physical Chemistry Chemical Physics*, 3:320-324, 2001.

56. J.J. Baschuk and X. Li, Modelling CO poisoning and O_2 bleeding in a PEM fuel cell anode, *International Journal of Energy Research*, 27:1095-1116, 2003.

57. N. Zamel and X. Li,Transient analysis of carbon monoxide poisoning and oxygen bleeding in a PEM fuel cell anode catalyst layer, *International Journal of Hydrogen Ener*gy, 33:1335-1344, 2008.

58. M. Murthy, M. Esayian, A. Hobson, S. MacKenzie, W. Lee, and J.W. Van Zee, Performance of a Polymer Electrolyte Membrane Fuel Cell Exposed to Transient CO Concentrations, *Journal of the Electrochemical Society*, 148:A1141-A1147, 2001.

59. S. Gottesfeld, and J. Pafford, A new approach to the problem of carbon monoxide poisoning in fuel cells operating at low temperatures, *Journal of the Electrochemical Society*, 135:2651-2652, 1988.

60. H. Dhar, L. Christner, A. Kush, Nature of CO adsorption during H_2 oxidation in relation to modeling for CO poisoning of a fuel cell anode, *Journal Electrochemical Society*, 134:3021-3026, 1987.

61. T.E. Springer, T.A. Zawadzinski and S. Gottesfeld, Modeling of polymer electrolyte fuel cell performance with reformate feed streams: effects of low levels of CO in hydrogen, *Symposium on*

Electrode Materials and Processes for Energy Conversion and Storage IV, Pennington, NJ: Electrochemical Society Inc., 1997.

62. W. Vogel, J. Lundquist, P. Ross and P. Stonehart, Reaction pathways and poisons-II: The rate controlling step for electrochemical oxidation of hydrogen on Pt in acid and poisoning of the reaction by CO, *Electrochimica Acta*, 20:79-93, 1975.

63. S. Jimenez, J. Soler, R.X. Valenzuela, L. Daza, Assessment of the performance of a PEMFC in the presence of CO, *Journal of Power Sour*ces, 151:69-73, 2005.

64. A. Rodrigues, J.C. Amphlett, R.F. Mann, Carbon Monoxide Poisoning of Proton-Exchange Membrane Fuel Cells, *Energy Conversion Engineering Conference*, Honolulu, HI, USA, 1997.

65. D. Brett, S. Atkins, N.P. Brandon, V. Vesovic, N. Vasileiadis, Investigation of reactant transport within a polymer electrolyte fuel cell using localised CO stripping voltammetry and adsorption transients, *Journal of Power Sources*, 133:205-213, 2004.

66. C. Wang, H. Chu, Transient analysis of multicomponent transport with carbon monoxide poisoning effect of a PEM fuel cell, *Journal of Power Sources*, 159:1025-1033, 2006.

67. D. Natarajan and T. Van, A Two-Dimensional, Two-Phase, Multicomponent, Transient Model for the Cathode of a Proton Exchange Membrane Fuel Cell Using Conventional Gas Distributors, *Journal of The Electrochemical Society*, 148:A1324-A1335, 2001.

68. Y. Wang, C. Wang, Transient analysis of polymer electrolyte fuel cells, *Electrochimica Acta*, 50:1307-1315, 2005.

69. N. Wagner, M. Schulze, Change of electrochemical impedance spectra during CO poisoing of the Pt and Pt-Ru anodes in a membrane fuel cell (PEFC), *Electrochimica Acta*, 48:3899-3907, 2003.

70. H. Chu, C. Wang, W. Liao, W. Yan, Transient behavior of CO poisoning of the anode catalyst layer of a PEM fuel cell. *Journal of Power Sources*, 159:1071-1077, 2006.

71. H. Wu, P. Berg, and X. Li, Modeling of PEMFC Transient with Finite-Rate Phase-Transfer Processes, *Journal of The Electrochemical Society*, 157:B1-B12, 2010.

72. H. Meng, Numerical investigation of transient responses of a PEM fuel cell using a two-phase non-isothermal mixed-domain model, *Journal of Power Sources*, 171:738-746, 2007.

73. N. Wagner and E. Gulzow, Change of electrochemical impedance spectra (EIS) with time during CO-poisoning of the Pt-anode in a membrane fuel cell, *Journal of Power Sources*, 127:341-347, 2004.

74. C.A. Schiller, F. Richter, E. Gulzow and N. Wagner, Relaxation impedance as a model for the deactivation mechanism of fuel cells due to carbon monoxide poisoning, *Physical Chemistry Chemical Physics*, 3:2113-2116, 2001.

75. C.A. Schiller, F. Richter, E. Gulzow and N. Wagner, Validation and evaluation of electrochemical impedance spectra of systems with states that change with time, *Physical Chemistry Chemical Physics*, 3:374-378, 2001.

76. J. Han, G.G. Park, Y.G. Yoon, T.H. Yang, W.Y. Lee and C.S. Kim, A new evaluation method of anode/cathode used for polymer electrolyte membrane fuel cell, *International Journal of Hydrogen Energy*, 28:609-613, 2003.

77. V. Gurau, F. Barbir, and H. Liu, An analytical solution of a half-cell model for PEM fuel cells, *Journal Electrochemical Society*, 147:2468-2477, 2000.

78. V. Gurau, H. Liu, and S. Kakac, Two-dimensional model for proton exchange membrane fuel cells, *AIChE Journal*, 44:2410-2422, 1998.

79. T.E. Springer, T.A. Zawodzinski, and S. Gottesfield, Polymer electrolyte fuel cell model, *Journal Electrochemical Society*, 138:2334-2342, 1991.

80. T. Zhou and H. Liu, A general three-dimensional model for proton exchange membrane fuel cell, *International Journal of Transport Phenomena*, 3:177-198, 2001.

81. C. Wang, Fundamental Models for Fuel Cell Engineering, *American Chemical Society*, 104:4727-4766, 2004.

82. A.Z. Weber and J. Newman, Modeling Transport in Polymer-Electrolyte Fuel Cells, *Chemical Rev.*, 104:4679-4726, 2004.

83. H. Wu, X. Li, P. Berg, On the modeling of water transport in polymer electrolyte membrane fuel cells, *Electrochimica Acta*, 54:6913-6927, 2009.

84. J.C. Amphlett, R.M. Baumert, R.F. Mann, B.A. Peppley, P.R. Roberge and T.J. Harris, Performance modeling of the Ballard Mark IV solid polymer electrolyte fuel cell, *Journal Electrochemical Society*, 142:1-8, 1995.

85. P.R. Pathapati, X. Xue, J. Tang, A new dynamic model for predicting transient phenomena in a PEM fuel cell system, *Renewable Energy*, 30:1-22, 2005.

86. J.T. Pukrushpan, H. Peng, and A.G. Stefanopoulou, Simulation and Analysis of Transient Fuel Cell System Performance Based on A Dynamic Reactant Flow Model, *ASME International Mechanical Engineering Congress & Exposition*, New Orleans, Louisiana, USA, 2002.

87. K. Sedghisigarchi, Dynamic and Transient Analysis of Power Distribution Systems With Fuel Cells – Part I: Fuel – Cell Dynamic Model, *IEEE Transactions on Energy Conversion*, 19:423-428, 2004.

88. J. Wang and R. Savinell, Simulation studies on the fuel electrode of a H_2-O_2 polymer electrolyte fuel cell, *Electrochimica Acta*, 37:2737-2745, 1992.

89. D. Bernardi and M. Verbrugge, Mathematical model of a gas diffusion electrode bonded to a polymer electrolyte, *AIChE Journal*, 37:1151-1163, 1991.

90. D. Bernardi and M. Verbrugge, A mathematical model of the solid-polymer-electrolyte fuel cell, *Journal of the Electrochemical Society*, 139:2477-2491, 1992.

91. T. Springer, M. Wilson, and S. Gottesfeld, Modeling and experimental diagnostics in polymer electrolyte fuel cells, *Journal of the Electrochemical Society*, 140:3513-3526, 1993.

92. S. Um and C. Wang, Three-dimensional analysis of transport and electrochemical reactions in polymer electrolyte fuel cells, *Journal of Power Sources*, 125:40-51, 2004.

93. K.K. Bhatia and C. Wang, Transient carbon monoxide poisoning of a polymer electrolyte fuel cell operating on diluted hydrogen feed, *Electrochimica Acta*, 49:2333-2341, 2004.

94. T. Berning, N. Djilali, A 3D, Multiphase, Multicomponent Model of the Cathode and Anode of a PEM Fuel Cell, *Journal of The Electrochemical Society*, 150:A1589-A1598, 2003.

95. J.J. Baschuk, Comprehensive, Consistent and Systematic Approach to the Mathematical Modeling of PEM Fuel Cells, *PhD thesis*, University of Waterloo, 2006.

96. M.M. Mench, *Fuel Cell Engines*, John Wiley & Sons, 2008.

97. S. Gilman, The mechanism of electrochemical oxidation of carbon monoxide and methanol on platinum II: the 'reactant pair' mechanism for electrochemical oxidation of carbon monoxide and methanol, *Journal of the Electrochemical Society*, 68:70-80, 1964.

98. T. Engel and G. Ertle, *The Chemical Physics of Solid Substances and Heterogeneous Catalysis*, edited by D.A. King, D.P. Woodruff, Elsevier, Amsterdam. 4:73-93, 1982.

99. P. Norton, *The Chemical Physics of Solid Substances and Heterogeneous Catalysis*, edited by D.A. King, D.P. Woodruff, Elsevier, Amsterdam, 4:27-72, 1982.

100. E-TEK Inc., *Gas Diffusion Electrodes Catalyst Materials Catalogue*, Naticks, MA, USA, 1995.

101. E. Gileadi, E. Kirowa-Eisner and J. Penciner, *Interfacial Electrochemisty: An Experimental Approach*, Addison-Wesley Pub. Co., 1975.

102. J. Wang and R. Samnell, Simulation studies on the fuel electrode of a H_2-O_2 polymer electrolyte fuel cell, *Ekctrochimica Acta*, 37:2737-274, 1992.

103. Y. Li, H. Wu, N. Zamel, X. Li, Multi-phase Multi-dimensional Analysis of the Effect of Fuel Quality on PEM Fuel Cell Performance, *SAE world congress conference*, Detroit, MI, USA, 2010.

104. H. Wu, X. Li and P. Berg, Numerical analysis of dynamic processes in fully humidified PEM fuel cells, *International Journal of Hydrogen Energy*, 32:2022-2031, 2007.

105. S. Lee, S. Mukerjee, E.A. Ticianelli, and J. McBreen, Electrocatalysis of CO tolerance in hydrogen oxidation reaction in PEM fuel cells, *Electrochimica Acta*, 44:3283-3293, 1999.